The Astronomical Journal, 168:103 (17pp), 2024 September https://doi.org/10.3847/1538-3881/ad5a99

Li Evolution among Stars of Low/Intermediate Mass: the Metal-deficient Open Cluster NGC 2204

Barbara J. Anthony-Twarog[1], Constantine P. Deliyannis[2], Aaron Steinhauer[3], Qinghui Sun[4,5], and Bruce A. Twarog[1]
[1] Department of Physics and Astronomy, University of Kansas, Lawrence, KS 66045-7582, USA; bjat@ku.edu, btwarog@ku.edu
[2] Department of Astronomy, Indiana University, Bloomington, IN 47405-7105, USA; cdeliyan@indiana.edu
[3] Department of Physics and Astronomy, State University of New York, Geneseo, NY 14454, USA; steinhau@geneseo.edu
[4] Tsung-Dao Lee Institute, Shanghai Jiao Tong University, Shanghai 200240, People's Republic of China; qinghuisun1@gmail.com
[5] Department of Astronomy, Tsinghua University, Beijing 100084, People's Republic of China
Received 2024 April 15; revised 2024 June 12; accepted 2024 June 12; published 2024 August 2

Abstract

We have analyzed high-dispersion spectra in the Li 6708 Å region for 167 stars within the anticenter cluster NGC 2204. From 105 probable members, abundance analysis of 45 evolved stars produces $[Fe/H] = -0.40 \pm 0.12$, $[Si/Fe] = 0.14 \pm 0.12$, $[Ca/Fe] = 0.29 \pm 0.07$, and $[Ni/Fe] = -0.12 \pm 0.10$, where quoted errors are standard deviations. With $E(B-V) = 0.07$ and $(m-M)_0 = 13.12$, appropriate isochrones provide an excellent match from the main sequence through the tip of the giant branch for an age of 1.85 ± 0.05 Gyr. Li spectrum synthesis produces A(Li) below 1.4 at the base of the red giant branch to a detectable value of −0.4 at the tip. Six probable asymptotic giant branch stars and all but one red clump star have only Li upper limits. A rapidly rotating red giant is identified as a possible Li-rich giant, assuming it is a red clump star. Main-sequence turnoff stars have a well-defined $A(\mathrm{Li}) = 2.83 \pm 0.03$ (sem) down to the Li-dip wall at the predicted mass of $1.29\,M_\odot$. Despite having the same isochronal age as the more metal-rich NGC 2506, the luminosity distribution of red giants reflects a younger morphology similar to NGC 7789, possibly indicating a deeper impact of metallicity on stellar structure and A(Li) than previously assumed. As in NGC 2506 and NGC 7789, the NGC 2204 turnoff exhibits a broad range of rotation speeds, making abundance estimation impossible for some stars. The place of the cluster within Galactic A(Li) evolution is discussed.

Unified Astronomy Thesaurus concepts: Open star clusters (1160); Stellar abundances (1577)

Materials only available in the online version of record: machine-readable table

1. Introduction

In a pioneering study, Hawarden (1975a) compiled a catalog of open clusters older than the Hyades using pseudo-color–magnitude diagrams to identify and categorize by age a large sample of previously unstudied open clusters observable from the Southern Hemisphere, noting a deficiency of older clusters in the direction of the Galactic center. For a subset of the newly categorized systems, including three of the oldest, NGC 2243 (Hawarden 1975b), Mel 66 (Hawarden 1976b), and NGC 2204 (Hawarden 1976a), Hawarden combined *UBV* photographic and photoelectric photometry to constrain the basic properties of each cluster from its two-color and color–magnitude diagrams (CMDs). Even with the photometric precision of nearly five decades past, it was readily discernible from the relative positions of the turnoffs and the well-populated giant branches that the clusters were significantly older than the Hyades and, for NGC 2243 and Mel 66, similar to or older than the canonically old open cluster, M67. For NGC 2204, the sparsely populated subgiant branch indicated an age roughly half that of M67, while $(U-B)$, $(B-V)$ two-color analysis suggested a modest reddening, $E(B-V) \sim 0.06$ to 0.08, and, critically, a $\delta(U-B)$-based metallicity comparable to that of Mel 66 but slightly higher than that of the clearly metal-deficient, anticenter cluster NGC 2243, which lies less than 15° south of NGC 2204. Any reasonable estimate of the distance of NGC 2204 placed it more than a kiloparsec above the Galactic plane, leading Hawarden (1976a) to classify the cluster as a potential halo, rather than disk, object.

Following an earlier analysis of the open cluster NGC 2420 (McClure et al. 1974), Hawarden's cluster program helped initiate a series of studies focused on anticenter clusters of intermediate age and subsolar metallicities (see, e.g., Mel 66: Anthony-Twarog et al. 1979; Ber 21: Christian & Janes 1979; NGC 2506: McClure et al. 1981; and NGC 2158: Christian et al. 1985), motivated in part by attempts to use the clusters to define the Galactic abundance gradient (e.g., Janes 1979).

Clusters including NGC 2420, NGC 2506, NGC 2204, and NGC 2243 are also studied to provide valuable insight into the role of metallicity in the evolution of stars of intermediate ($1.6\,M_\odot$) to low ($0.9\,M_\odot$) mass. From an observational standpoint, NGC 2204 has presented some challenges that have reduced its popularity for programs devoted to anticenter clusters of lower metallicity. It is more distant and significantly less populous than better studied systems such as NGC 2420 and NGC 2506, and is neither as old nor as metal-poor as Mel 66 and NGC 2243. Astrometric isolation of members from the rich foreground field has become easier (see, e.g., Dias et al. 2014; Cantat-Gaudin et al. 2018) only recently, while high-precision radial velocity studies of the cluster have reached barely below the level of the red giant clump (Mermilliod & Mayor 2007).

Despite these challenges, NGC 2204 was included in our ongoing program to delineate the impact of metallicity, age, and stellar rotation on the evolution of Li among stars of intermediate-to-low mass (see Anthony-Twarog et al. 2021;

Sun et al. 2022 and references therein). As discussed extensively in Deliyannis et al. (2019), clusters with ages in the 2–4 Gyr range are likely to have main-sequence turnoff (MSTO) stars exhibiting Li depletion while unevolved, if their masses placed them in the main-sequence Li-dip (Boesgaard & Tripicco 1986). However, the MSTO stars above (more massive than) the Li-dip may show varying levels of Li depletion, even before cooling and expansion on the subgiant and giant branches lead to its depletion through dilution due to the deepening of the surface convection zone, and other possible effects (Twarog et al. 2020). As giants, the stars will be low enough in mass ($\leqslant 2\ M_{\odot}$) to experience a disruptive ignition of helium at the tip of the red giant branch (RGB). Despite the general diminution of Li between the MSTO and giant branch tip, a small number of cluster giants show measurable, and in some cases abundant, levels of surface Li (see, e.g., Carlberg et al. 2016). Since the mass range of the Li-dip is particularly sensitive to metallicity (Cummings et al. 2012; Anthony-Twarog et al. 2021), the combination of cluster age and lower metallicity for NGC 2204 implied that the stars leaving the main sequence in this cluster would be on the hot side of the Li-dip and potentially could still retain the signature of their primordial cluster Li abundance, thereby supplying a constraint for both stellar and Galactic chemical evolution.

The goal of the current investigation is to present the results of a spectroscopic survey of NGC 2204 stars from the tip of its extended giant branch to the MSTO, reaching to the level of the Li-dip. Section 2 details the experimental design and data acquisition for our spectroscopic observations. Section 3 updates the status of cluster membership and possible binarity for the stars of interest, while Section 4 reviews the evidence from prior studies pertaining to the cluster's age, reddening, and metal abundance. Section 5 presents the metallicity determination from the Hydra spectra, which is followed in Section 6 by the determination of the Li abundances and their contribution to our understanding of stellar and Galactic Li. Section 7 contains a summary of our conclusions.

In the following discussions and tables, individual stars will be referenced by their WIYN Open Cluster Survey (WOCS) numbers, assigned in a forthcoming photometric survey by A. Steinhauer et al. (2024, in preparation; SD24). Where available, identifications from WEBDA will also be included with a "W" prefix; these identifications are in most cases taken from Hawarden (1976a) and are the most common identifier in earlier studies of the cluster.

2. Experimental Design: Sample Selection and Data Acquisition

2.1. Original Sample Selection

Our spectroscopic sample was constructed in 2014, so without the insight subsequently provided by Gaia astrometric, kinematic, and photometric data (Gaia Collaboration et al. 2016, 2018 DR2, 2023 DR3). A primary goal was the delineation of Li abundance as stars evolve from the hot side of the Li-dip to the base of the giant branch, as exemplified by the analysis of NGC 2506 (Anthony-Twarog et al. 2018b).

The extensive radial velocity survey of Mermilliod & Mayor (2007) provided an important guide for choosing candidate giant members, as their original discrimination between single members and binary and/or nonmember stars was excellent. Our MSTO candidate list was chosen based on a limited set of instrumental extended Strömgren photometry obtained at the same time as the photometric survey of NGC 2506 (Anthony-Twarog et al. 2016). For the subgiant branch, however, photometric isolation of likely members proved difficult, so all stars within a plausible (V, ($B-V$)) range were observed in the hope of identifying a handful of possible subgiants.

With the hindsight that Gaia results have provided, it is made clear in Section 3 that this approach worked well to select stars with joint photometric similarities of temperature and metallicity along the nearly vertical turnoff, but confirmed the minimal presence of member stars within the Hertzsprung gap.

2.2. Hydra Data Acquisition

Spectra for 167 stars in the field of NGC 2204 were obtained in 2014 and 2015 using the Hydra multiobject spectrograph on the WIYN 3.5 m telescope. To cover different magnitude ranges of candidate stars, four separate fiber configurations were developed, the brightest of which incorporated only two stars with $V \leqslant 12$. This configuration was observed in two exposures on 2014 January 26 (UT date) for 30 minutes total. A second configuration covered 45 additional giants to $V = 14$ and was observed in three exposures for 2.6 hr on 2014 February 25. Two additional configurations were designed for fainter stars and required observations in 2014 February and 2015 January. A configuration incorporating 61 stars, largely subgiant candidates, was observed for nearly eight hours on 2014 January 25 and 2015 February 20, with the final and faintest configuration of 59 MSTO candidates receiving over 16 hours of exposure on 2014 February 27 and 2015 January 18 and 19. We note that our fiber configurations also incorporated dozens of unassigned fibers from which simultaneous spectra can be used for sky subtraction.

The adopted spectrograph setup produces spectra centered on 6650 Å with a dispersion of 0.2 Å per pixel and a range of ~400 Å. Examination of thorium–argon lamp spectra, used for wavelength calibration, indicates lines 2.5 pixels wide, yielding an effective spectral resolution of 13,300. In addition to longer Th–Ar lamp spectra obtained during the day, comparison lamp spectra were obtained before and after object exposures in the course of the night. Except for radial velocity standards observed throughout the night, comparison lamp spectra, dome flats, and daytime sky spectra were obtained with the same fiber configurations used for program observations. These daytime solar spectra were used to correct for fiber-to-fiber throughput differences, as well as to provide reference solar spectra to zero the log gf values of individual lines required to reproduce solar abundances.

Our IRAF[6]-based processing steps have been described in past papers (see, e.g., Anthony-Twarog et al. 2018a, 2018b, 2021; Deliyannis et al. 2019) and include the typical application of bias subtraction, flat-fielding using dome flats for each configuration, and wavelength calibration using comparison lamp exposures. Our strategy for cosmic-ray cleaning uses "L. A. Cosmic"[7] on the long-exposure frames after the flat-field division step. Final composite spectra were obtained by coaddition of multiple exposures to obtain the highest possible signal-to-noise per pixel ratio (S/N). The

[6] IRAF is distributed by the National Optical Astronomy Observatory, which is operated by the Association of Universities for Research in Astronomy, Inc., under cooperative agreement with the National Science Foundation.

[7] http://www.astro.yale.edu/dokkum/lacosmic/, an IRAF script developed by P. van Dokkum (2001); spectroscopic version.

combination of spectra from 2014 and 2015 was completed only after inspection for possible radial velocity variability. One star has a noticeable wavelength shift over the year-long interval and will be noted in a subsequent table with separate velocity estimates based on individual rather than summed data sets.

Since the goal of coaddition is to obtain higher-S/N spectra, it is worth noting how that parameter may be estimated and what the resulting values mean. One criterion estimates the total flux per pixel above sky before continuum fitting, an indication of the total signal accumulated for a star. The square root of this quantity provides a fair estimate of the accumulated flux-based S/N. Another method measures the actual variance of the spectrum in a line-free region. Even in a relatively metal-poor star, such a region is hard to come by and tends to be relatively small; in the current case, the region between 6680 and 6690 Å was selected for this purpose. For the cooler giant stars these latter S/N estimates, derived using *splot* in IRAF, are significantly smaller than the flux-based estimators by factors as large as dozens, primarily because numerous difficult-to-separate weak lines begin to appear, making a line-free region difficult to identify. The flux-based S/N will be adopted in all further discussions. Other than one MSTO star with $S/N = 83$ due to a single epoch of observation, all stars had S/N in excess of 100. A few luminous red giants (RGs) have coadded spectra with S/N over 700. For the 105 members, the median S/N value is 217.

The Fourier-transform, cross-correlation utility *fxcor* in IRAF was used to assess kinematic information for each star from the summed composite spectra. In *fxcor*, program stars are compared to zero-velocity stellar templates of similar $T_{\rm eff}$. Templates are usable for spectral types F5 through K6, making this technique less effective for the reddest members of NGC 2204. The *fxcor* utility characterizes the cross-correlation-function (CCF), from which estimates of each star's radial velocity are easily inferred. Formal errors implied by the CCF analysis with *fxcor* suggest that typical formal $V_{\rm RAD}$ errors are $\sim$1 km s^{-1}. We were in a position to test this more formally as two stars were observed in duplicate configurations straddling the two years of our survey. Discrepancies within those year-to-year and configuration-to-configuration comparisons were well under 1 km s^{-1} for the two stars. Radial velocity standards were observed every night of the 2014/2015 observing runs, ideally in the same configuration and time-adjacent to the program observations. In all, observations of six standards on five separate nights generated the 16 individual radial velocity measures used to zero the *fxcor*-derived radial velocities to the standard system to within 1.0 km s^{-1}.

Rotational velocities can also be estimated from the CCF FWHM using a procedure developed by Steinhauer (2003). We note here that although we will refer to rotational velocities, the measurements in fact yield projected rotational velocities $V_{\sin i}$. Our method exploits the relationship between the CCF FWHM, line widths, and $v_{\rm ROT}$, using a set of numerically "spun up" standard spectra with comparable spectral types to constrain the relationship. Our previous analyses of both red giant and turnoff spectra demonstrate that *fxcor* cross-correlation profiles have significantly reduced accuracy when attempting to reproduce rotational velocities above 35 km s^{-1}. We note that spectral resolution alone implies that derived projected rotational velocities below $\sim$15 km s^{-1} are not meaningful, a result confirmed in past analyses (see, e.g., Deliyannis et al. 2019). With the exception of stars likely to be binaries, the derived mean projected rotational velocities are unexceptional: 14.7 ± 3.5 km s^{-1} for the RG and subgiant (SG) members not identified as photometric or $V_{\rm RAD}$ variables in other surveys, implying that, as expected for evolved stars, the stars have spun down to minimal rotation speeds. MSTO stars not designated as potential binary or wide-lined show an average $v_{\rm ROT} = 25.5 \pm 10.5$ km s^{-1}. By contrast, MSTO stars flagged as potential binaries and/or wide-lined based on visual examination of spectra show predictably larger average $v_{\rm ROT}$ values of 34.3 ± 15.4 km s^{-1}.

2.3. External Sources of Spectra

We close this section by noting additional spectra for four giant members of NGC 2204, accessed from the ESO Science Archive Facility for comparison and analysis. These spectra had been obtained for program ID 167.D-0173, PI R. Gratton in 2001 October. The spectra, with S/N ranging from 116 to 179, were obtained with the Fibre Large Array Multi Element Spectrograph fiber-feed assembly to the high-resolution UVES spectrograph with pixel resolutions of 16.9 mÅ.

3. Cluster Membership and Binarity

3.1. Astrometry

For membership purposes, the first phase of estimation comes from the astrometric contribution supplied by the proper motion and parallax, exquisitely measured by the ongoing Gaia collaboration. The first comprehensive analysis of the Gaia data for clusters was compiled by Cantat-Gaudin et al. (2018, CG18), with periodic updates since then (Cantat-Gaudin et al. 2020, CG20).

While all nonzero membership probabilities for stars within NGC 2204 were available from CG18, to protect against omission of potential members at large radial distance from the cluster center or those tagged as zero-probability members due to other anomalies such as poor astrometric measure, we adopted a process of membership discrimination similar to that used in the much richer but less distant cluster M67 (Twarog et al. 2023). As a baseline, we made use of the cluster membership survey by CG18, tied to the DR2 data release. Necessary first steps involved cross-matching of *BV* photometric indices from SD24 with cluster membership lists from CG18 and the raw data from Gaia DR3. For a few spectroscopic candidates that fall outside the SD24 field of study, Gaia synthetic photometric values (GSPC; Gaia Collaboration et al. 2022) for *V* and *B* have been used.

It was initially assumed that absence of a star from the original CG18 member compilation implied nonmembership, though, as noted, the possibility existed that stars with larger than typical astrometric errors could be incorrectly excluded from the cluster database. Since astrometric data for all sample stars are readily accessible in the DR3 data, "nonmembership" for stars not tagged as members by CG18 has been quantified as follows. 572 stars in NGC 2204 classified as members with a probability higher than 50% (CG18) were identified in DR3. Using only 258 stars from DR3 with $\pi/\sigma_\pi \geqslant 5$, mean cluster values in π and proper motion were derived, generating $\pi = 0.224 \pm 0.041$ mas, $\mu_\alpha = -0.575 \pm 0.081$ mas yr^{-1}, and $\mu_\delta = 1.958 \pm 0.072$ mas yr^{-1}, where the quoted errors refer to the standard deviations about the mean. For each observed candidate star in DR3, a quantity QM (quality metric) was constructed from the square root of the quadratic sum of the

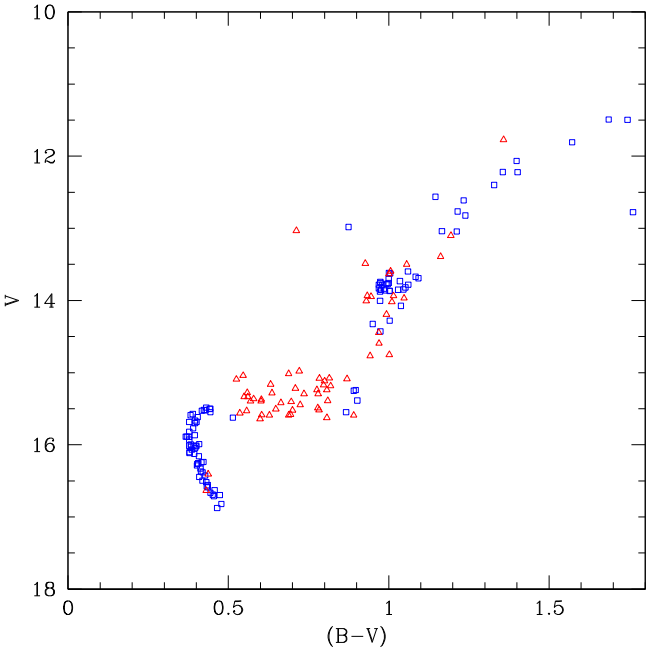

Figure 1. CMD of the preselected sample of 167 stars in NGC 2204. Ultimate membership decisions are reflected by symbol: blue squares for probable members, red triangles for nonmembers.

number of standard deviations that that star's π, μ_α, and μ_δ are from the mean values. Stars classified as members from the CG18 compilation have QM of 10 or less within DR3, i.e., probable member stars are less than 10σ in all three astrometric dimensions from the cluster mean parameter values. Stars in our target sample that are not included in either CG18 or CG20, and are thus likely nonmembers, have QM values from 11.5 to as high as 2000.

Figure 1 illustrates the CMD location of the Hydra sample stars; symbol colors and shapes reflect the subsequent separation into members and nonmembers, based purely on astrometric criteria. Our original photometrically based member selection was extremely successful for the MSTO region, although it necessarily short-changed the more interesting aspects of the blue hook morphology associated with the phase of rapid hydrogen exhaustion (see the isochrones of Figure 4 between $V = 14.8$ and 15.2) to maintain a sample of easily identifiable stars on the vertical turnoff. With decades of prior radial velocity observations to guide our sample selection of giants, that configuration, too, was largely successful in tagging member stars as targets. Our attempt to study the meager subgiant branch, however, was primarily unsuccessful. As will be discussed in Section 6, this deficiency of stars on the horizontal subgiant branch is real and is a strong indicator of the relative youth of NGC 2204 compared to the 3.6 and 3.7 Gyr old clusters NGC 2243 (Anthony-Twarog et al. 2021) and M67 (Twarog et al. 2023). From the more complete astrometric sample of Figure 4 and excluding stars that lie well off the isochrone sequence, eight stars are positioned between the MSTO and the red giant clump (RGC); our spectroscopic sample includes five of these, primarily those at the base of the vertical first-ascent RG branch.

3.2. Radial Velocity Determination: Current and Past

Results based on *fxcor* for the MSTO stars in a metal-poor cluster such as NGC 2204 can be challenging. Several contributing factors such as rotation and/or binarity might conspire to broaden and blur the already relatively weak lines. Although our spectra are of more than adequate S/N per pixel, *fxcor* struggled with weak and apparently washed out lines. For many such MSTO stars, velocities are reported, but the larger than usual formal errors indicate where the results are less reliable.

Although not directly used as a membership discriminant, our radial velocity data consistently support the astrometric separation into members and nonmembers. For the 105 stars ultimately classed as astrometric members, the mean radial velocity is 92.5 ± 11.3 km s^{-1}; the larger than average dispersion is likely due to the contribution of binaries that have not been identified and eliminated from the sample, as well as the uncertainty added by rapid rotators with broadened lines. The velocities for the designated nonmembers are gratifyingly distinct: 41.75 ± 40.0 km s^{-1}. For our best estimate of the cluster radial velocity, we can eliminate six stars (see discussion below) previously identified as spectroscopic binaries, plus the star WOCS5015, which, while an astrometric member, has a radial velocity, confirmed by Gaia, near 21 km s^{-1}. For the 99 remaining stars, the mean radial velocity becomes 92.45 ± 8.18 km s^{-1}, still a disturbingly large scatter. The source of the problem becomes obvious when the sample is reduced to only red giants and subgiants, stars with intrinsically narrow lines. For these 42 stars, the cluster mean becomes 90.9 ± 1.94 km s^{-1}. The fact that the dominant source of the scatter in the original cluster mean comes from broad-lined stars at the turnoff is confirmed by the direct comparison between our individual radial velocities and those from past research, usually on evolved stars, where the scatter in the offset residuals is typically 0.7–2.8 km s^{-1} (see discussion below).

Although still quite important in the context of membership discrimination, radial velocity plays a growing role in the identification of potential variable and binary systems by highlighting departures from cluster mean properties. A review of past radial velocity surveys will set up a discussion of our survey results and comparisons.

Jacobson et al. (2011) summarize the various attempts made before 2000 to define the cluster mean radial velocity, including Friel et al. (2002) who observed 19 red giant candidates, seven of which were classified as nonmembers or possible nonmembers. Friel et al. (2002) found a mean cluster velocity of 89 ± 6 km s^{-1}.

Mermilliod & Mayor (2007) published velocities for giants in several open clusters based on observations with the CORAVEL instrument at the Danish 1.5 m telescope at La Silla, Chile, including 35 stars in NGC 2204. Ten stars were identified as nonmembers, with an additional handful of stars flagged as spectroscopic binary candidates, several of which will be discussed in greater detail below. From the single-star candidate members, a mean radial velocity of 91.38 km s^{-1} was obtained, with an rms error of 1.33 km s^{-1}. Mermilliod & Mayor (2007) noted the agreement within the errors with the earlier, less precise result of Friel et al. (2002).

Jacobson et al. (2011) conducted a Hydra II-based survey of 35 stars in NGC 2204, obtained at the 4 m Blanco telescope at CTIO. Based on 16 stars, they derived a mean radial velocity of 88.4 ± 1.3 km s^{-1}. An additional ground-based spectroscopic survey of interest is that of Carlberg et al. (2016), supplying radial velocities for NGC 2204 based on spectra obtained with the MIKE instrument at Magellan with $R \sim 31{,}000$–$44{,}000$. From an original data set of 19 candidate evolved stars,

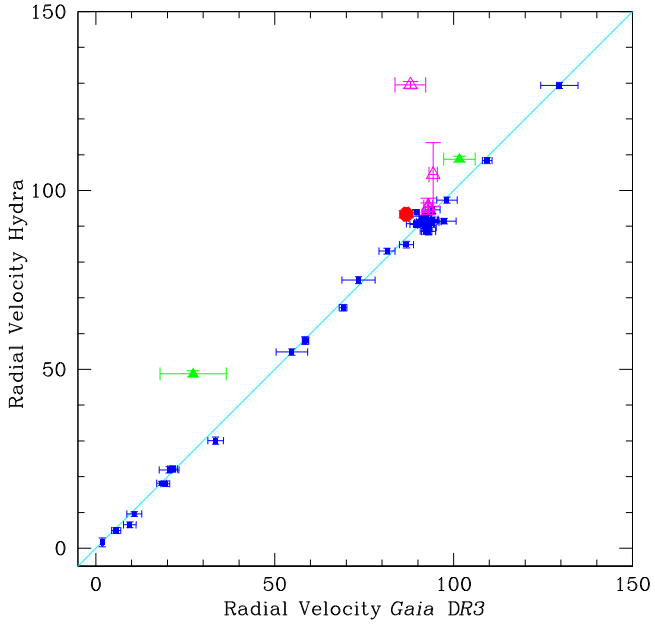

Figure 2. Comparison of Hydra and Gaia DR3 radial velocities. The cyan line is not a fit, merely an illustration of one-to-one correspondence. A single red filled symbol shows WOCS1002, denoted by Mermilliod & Mayor (2007) as an SB. Possible SBs WOCS1005, WOCS2006, WOCS1003, and WOCS4014 are denoted by magenta open triangles. Two green solid triangles show the positions of WOCS9015 and WOCS8011 while the blue squares represent the remaining comparisons between Hydra and DR3 radial velocities.

Carlberg et al. (2016) excluded two stars, WOCS1003 = W4119 and WOCS8011 = W2330, as a potential binary and nonmember respectively to arrive at an average radial velocity of 91.12 ± 1.22 km s^{-1}, where the quoted error describes the standard deviation for the set.

Finally, the recent publication of Gaia DR3 data provides a large set of well characterized radial velocities to which our Hydra values are compared in Figure 2 for 64 stars in common. Although the most recent data release does not explicitly flag stars for radial velocity variability, candidate binaries might be identified when compared with data from other sources and epochs. Some of the features of Figure 2 refer to stars flagged as potential spectroscopic binary (SB) systems in earlier studies or by the present work.

In summary, after eliminating seven stars from our sample that exhibit evidence for $V_{\rm RAD}$ variability (see Section 3.3 below), comparison of our Hydra $V_{\rm RAD}$ results with past surveys produces the following systemic differences. With respect to Friel et al. (2002), our results for 11 stars in common are 1.57 ± 5.65 km s^{-1} larger; based on 18 stars in common with Jacobson et al. (2011), our $V_{\rm RAD}$ values are 2.80 ± 2.73 km s^{-1} larger. With respect to Mermilliod & Mayor (2007), the difference in the same sense of (HYDRA —survey) is -0.26 ± 2.11 km s^{-1}, based on 20 stars in common. Finally, comparing to values for 17 stars from Carlberg et al. (2016), the difference is -0.11 ± 0.74 km s^{-1}. Even with the exclusion of seven potentially variable-velocity stars, 57 stars remain in common between the Hydra sample and results from DR3, for which the average difference (HYDRA – DR3) is -1.03 ± 1.69 km s^{-1}. Typical velocity errors for these data sets are 0.92 ± 0.25 km s^{-1} for Hydra values and 1.73 ± 1.10 for DR3 values.

3.3. Radial Velocity Variables and Binarity

Mermilliod & Mayor (2007) identified one star as a clear SB, WOCS1002 = W1129, identified in Figure 2 by a large red filled circle. In spite of a high probability of membership in CG18, its Gaia DR3 velocity is offset both from the cluster mean and the Hydra value by more than 6 km s^{-1}. Four other stars (WOCS1005 = W4132, WOCS2006 = W1136, WOCS4014 = W3304, WOCS1003 = W4119) were flagged by Mermilliod & Mayor (2007) as potential spectroscopic binaries and are noted in Figure 2 with open magenta triangles. WOCS1005 is a very cool giant near the bending tip of the RGB. Identified as an L nonperiodic variable by ASAS-SN (Shappee et al. 2014),[8] the star is also flagged as a variable in DR3. Our Hydra-based radial velocity was based only on the Hα line, resulting in a large formal error for that value: 104.5 ± 8.9 km s^{-1} compared with a DR3 value of 94.3 ± 1.16 km s^{-1}. Like WOCS1005, WOCS2006 also has an extremely red $(B - V)$ color, is flagged as a photometric variable in DR3, and has been classified by ASAS-SN as a semi-regular variable with a period of 59.4 days. The remaining two stars flagged by Mermilliod & Mayor (2007) as possible SBs inhabit less extreme locations along the RGB. WOCS4014 and WOCS1003 were both noted as a potential SBs by Jacobson et al. (2011). As mentioned above, WOCS1003 was also identified as a spectroscopic binary by Carlberg et al. (2016). Although only observed in 2014 in our Hydra survey, our result is consistent with a spectroscopic binary classification for the star. The 2014 $V_{\rm RAD} = 129.5 \pm 0.9$ km s^{-1} may be compared to the Gaia (Gaia Collaboration et al. 2018, DR2) value of 80.0 ± 1.5 km s^{-1} and the DR3 result of 87.9 ± 4.3 km s^{-1}, supporting a case for $V_{\rm RAD}$ variability for this star. The large error for the DR3 results may in itself be indicative of variability within the composite sets of data comprising this final value.

Returning to the case of WOCS8011 = W2330, noted by Carlberg et al. (2016) as a potential radial velocity nonmember with $V_{\rm RAD}$ of 96.5 km s^{-1}, we note some evidence of radial velocity variability in our results and those culled from DR3. Our Hydra value of 108.8 ± 0.8 km s^{-1} is similar to the DR3 value of 101.6 ± 4.4 km s^{-1} but even more widely separated from the cluster mean. We identify this star as a possible SB.

Although not found in any other $V_{\rm RAD}$ survey, results for WOCS11733 indicate it to be a nonmember and potential radial velocity variable. The separate Hydra observations in 2014 (44.3 ± 1.5 km s^{-1}) and 2015 (83.3 ± 0.7 km s^{-1}) imply binarity. This star will not be considered further, as both astrometry and the $V_{\rm RAD}$ values indicate nonmembership. One more radial velocity variable candidate is found among the apparent nonmembers. Star WOCS9015 = W1308 appears among the fainter RGB stars but has radial velocity measures that suggest nonmembership and potential binarity; the value recorded by Gaia DR3 is 48.73 km s^{-1} with a typical error. Our Hydra measurement is considerably smaller, 27.2 km s^{-1}, but with an atypically large error of 9.24 km s^{-1}. Astrometry from Gaia, discussed below, supports nonmembership for the star. These two stars are represented in Figure 2 by filled green triangles.

[8] https://asas-sn.osu.edu/variables

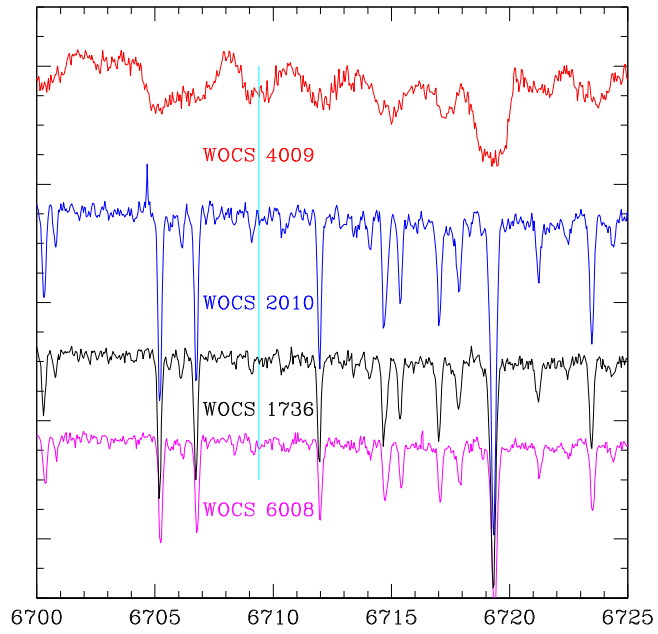

Figure 3. VLT spectra in the Li line region for four giant members of NGC 2204, including the apparently rapid rotator W4216 = WOCS4009. For this figure, the spectrum of WOCS4009 has been offset by 0.7 Å to the blue, equivalent to a $\sim$30 km s^{-1} offset to align its spectrum with the other three. The vertical cyan line indicates the expected location of the Li line, 9.9 Å to the blue of the Ca 6717 Å line.

3.4. Indications of Variability or Binarity from Photometry

Many open clusters have been closely observed for main-sequence variable candidates by J. Kaluzny and collaborators, including NGC 2204 (Rozyczka et al. 2007). Six variable candidates were identified in the cluster, of which two are bright enough to have been included in the present study. The group's temporal coverage was sufficient to establish light curves and classifications for all six candidates. The brighter candidate (their number 438, V0402 CMa, WOCS5002) is classed as a detached, circularized eclipsing binary with a period of nearly seven days. The other candidate (226, V0403 CMa, WOCS20010, W2216) may be an ellipsoidal variable with a period $\geqslant$2 days. Both stars are highly probable members according to CG18, and one of the two (WOCS20010) is in our Hydra sample.

The ASAS-SN database was also probed for variables, identifying nine candidates with $V \leqslant 17$ and within 20′ of the center of NGC 2204. Of the nine, four are not in the CG18 membership list; two others are identical to the two variable candidates identified by Rozyczka et al. (2007). The remaining three are evolved stars, including two of the reddest stars among the giants of NGC 2204. WOCS1005 = W4132 and WOCS2006 = W1136 have $(B-V)$ colors redder than 1.7. WOCS1005 is not in the CG20 member list but its astrometric properties suggest that it is a possible member. ASAS-SN describes it as nonperiodic L-type variable. WOCS2006 is a likely member with a period of 59 days and was noted initially by Hawarden (1976a) as a semi-regular variable distinctive for its position below the main giant branch.

The final ASAS-SN-designated variable candidate is WOCS4009 = W4216, denoted as a rotational variable, i.e., a star with variable brightness probably due to its rotation coupled with a nonuniform surface brightness, with a period of 6.18 days. Its astrometric parameters indicate that it is a member with a CMD location near the RGB clump. Spectra for the four giants observed by the Very Large Telescope (VLT) are shown in Figure 3, where the unusual breadth of WOCS4009 is easily noted, as is its velocity offset of $\sim$30 km s^{-1} from the other three giants.

Among the Gaia data products released in DR3 is a photometric variability flag. The three giants included among the Gaia variable candidates are the same stars similarly flagged by ASAS-SN. An additional half dozen MSTO members are among the stars flagged for variability, including the star identified by Rozyczka et al. (2007) as an ellipsoidal variable, WOCS20010.

Table 1 contains a summary of our basic information for the 167 stars included in the spectroscopic survey, comprising 105 members and 62 likely nonmembers. The columns in Table 1 include the IDs, if available, from WEBDA (Hawarden 1976a) as well as WOCS numbers. A handful of stars are outside the area covered by SD24 and are noted by letters A through E in the complete Table 1. Also listed are (α, δ) for each star from DR3, V and $(B-V)$ from the broadband photometric survey by SD24 or synthesized photometry from Gaia, our derived radial velocity with errors, and our assessment of membership status.

4. Preliminary Cluster Properties: Reddening, Metallicity, Age

The analysis and interpretation of our spectra will require knowledge or assumptions about the cluster's bulk properties of foreground reddening, $E(B-V)$, metallicity, and age so that atmospheric parameters needed to construct model atmospheres may be matched to the stars' $T_{\rm eff}$ and log g values, the latter estimated by comparisons of photometric values to well-matched isochrones. Precise, extensive, and deep photometry is therefore necessary. We utilize photometric colors to estimate $T_{\rm eff}$ using a color–temperature relation that also depends on $E(B-V)$ and [Fe/H] estimates. Contributions from past studies that are most relevant to determinations of $E(B-V)$ and [Fe/H] are summarized below. Where appropriate, conclusions from these prior studies have been reevaluated in the light of astrometric information on membership.

Hawarden (1976a) provided early evidence for NGC 2204's status among metal-poor, lightly reddened, and intermediate-age open clusters. More than two decades would pass until deeper and wider-field photometric surveys would supersede that work, but evidence for the modest foreground reddening and metal paucity of the cluster continued to reinforce Hawarden's basic conclusions, including a photoelectric David Dunlap Observatory (DDO) study by Dawson (1981). For six of the stars observed by Dawson (1981), internally consistent photoelectric techniques permitted a reddening estimate of $E(B-V) = 0.08 \pm 0.01$. Reanalysis of the DDO sample using five probable members by Twarog et al. (1997) led to $E(B-V) = 0.08$ and [Fe/H] $= -0.34 \pm 0.25$ (sd).

In the hindsight enabled by Gaia, several of the stars used by Dawson are not found in the cluster membership list assembled by CG18. Inspection of the derived reddening and δCN parameters for six probable members as derived in the current analysis suggests an average $E(B-V) = 0.04 \pm 0.07$ and [Fe/H] $= -0.53 \pm 0.34$, citing simple standard deviations among the separate stars' estimates. The DDO estimator of metallicity is based on δCN and thus might be better viewed as an estimate of [m/H] rather than one of a purely iron-peak abundance but, given the large dispersion, it is of little fundamental value.

A deep and extensive *BVI* CCD survey of NGC 2204 was published by Kassis et al. (1997), which incorporated

Table 1
Hydra Sample

α(DR3)	δ(DR3)	WOCS	WEBDA	V	$(B-V)$	Status	V_{RAD}	σ_{Vrad}	Notes
93.90276	−18.78131	2014	3325	11.491	1.686	M	91.22	2.33	(8)
93.88815	−18.70460	1005	4132	11.495	1.745	M	104.48	8.87	(4) A, G; (7) H, MM-SB?; (8); (9) (Note a)
94.08091	−18.83833	1732	⋯	11.771	1.358	N	1.65	1.25	⋯
93.88085	−18.71567	1006	4137	11.806	1.572	M	89.31	1.71	(4)
93.74355	−18.64528	1017	⋯	12.065	1.399	M	91.36	1.06	⋯
93.70613	−18.52075	1028	⋯	12.220	1.356	M	91.81	1.02	(9)
93.99237	−18.67401	4014	3304	12.221	1.402	M	95.24	1.30	(6); (7) MM-SB?
94.08265	−18.77434	2028	⋯	12.400	1.329	M	91.18	1.00	(9)
93.83926	−18.59759	1011	1320	12.562	1.146	M	90.97	0.88	(8)
93.88300	−18.66028	1002	1129	12.613	1.234	M	93.36	1.03	(7) MM- SB
93.95708	−18.62761	3011	2212	12.766	1.215	M	91.39	0.95	(6)
93.87297	−18.62536	2006	1136	12.777	1.762	M	95.57	2.29	(4) A,G,H; (7) MM-SB?; (8); (9)
93.91828	−18.77696	6014	3324	12.822	1.239	M	90.84	0.98	⋯
93.94558	−18.63205	2009	2211	12.982	0.875	M	91.52	0.85	(5); (8)
93.91942	−18.76232	1012	⋯	13.032	0.712	N	18.16	0.53	(4) G; (8); (9)

Notes. (1) Star is outside photometric survey area, V and $B-V$ synthesized from Gaia DR3 GSPC. (2) Only VLT spectrum. (3) Also VLT spectrum. (4) Photometric variability designated by Gaia (G), Hawarden (H), Rozyczka et al. (2007) (K) or ASAS-SN (A). (5) DR3 indicates nonsingle star; (6) Reported radial velocity is an average from two epochs and/or configurations; reported error is the average of each epoch's formal error. (7) Radial velocity variation detected from Hydra spectra or reported by Mermilliod & Mayor (2007, MM). (8) Gaia magnitude g and V appear discrepant. (9) Gaia renormalized unit weight error significantly different from 1.0. (10) No astrometry in DR3.

Individual notes: (a) Hydra radial velocity estimated from Hα only; (b) V_{RAD} variability suggested by comparison to DR2 (79.96 ± 1.34 km s^{-1}) and DR3 (87.94 ± 4.29 km s^{-1}); (c) V_{RAD} variability for WOCS4009 suggested by VLT offset and DR3 value; (d) V_{RAD} values for WOCS11733 in 2014 and 2015 are respectively 44.34 ± 1.46 km s^{-1} and 83.3 ± 0.74 km s^{-1}; (e) WOCS24009 reports single epoch only.

(This table is available in its entirety in machine-readable form in the online article.)

comparisons of BV and VI CMDs to isochrones from Bertelli et al. (1994). While independent determinations of reddening and metallicity were not attempted, some exploration of the interdependence of age, metallicity, and reddening was presented for subsolar metallicities, ages between 1.3 and 2.5 Gyr, and reddening values below $E(B-V) = 0.2$. Given that the isochrones used have been superseded by more recent models, the absolute values obtained are of questionable value.

It should be noted that independent estimates for $E(B-V)$, i.e., those that do not depend on photometry or spectroscopy, are available based on dust emission/reddening maps by Schlegel et al. (1998) and Schlafly & Finkbeiner (2011). The maximum reddening in the direction of NGC 2204 is $E(B-V) = 0.08$–0.09 based on Schlafly & Finkbeiner (2011).

In spectroscopic surveys aimed at abundance determination, reddening-corrected photometric colors are often used with an assumed value for $E(B-V)$ and a color–temperature calibration to provide values or starting estimates for $T_{\rm eff}$. Such was the case for Jacobson et al. (2011), who adopted a reddening value $E(B-V) = 0.08$ (essentially unchanged from Hawarden 1976a) to derive [Fe/H] $= -0.23 \pm 0.04$ from 13 cluster members. This is higher than but within the errors of the previous result from Friel et al. (2002), [Fe/H] $= -0.32 \pm 0.10$ based on somewhat lower-resolution spectra. Spectra for both studies were obtained at CTIO, with the 2011 data obtained using the southern analog of the Hydra instrument used for the present study and in the same wavelength region.

SD24 compiled *UBVRI* photometry for over 3800 stars in the field of NGC 2204, centered on (α, $\delta = 93\overset{\circ}{.}882$, $-18\overset{\circ}{.}650$) using the Half-Degree Imager at the WIYN[9] 0.9 m telescope on Kitt Peak. Their analysis of the CMD and color–color diagrams led to estimates for NGC 2204's age of 2.2 ± 0.1 Gyr, foreground reddening $E(B-V) = 0.08 \pm 0.01$, and [Fe/H] $= -0.45 \pm 0.05$, based on comparison to Yale–Yonsei (Demarque et al. 2004) isochrones. This survey provides the base BV photometry used in our analysis to develop estimates of atmospheric parameters. For a small subset of stars with spectroscopy that lie outside the SD24 survey field, extensive synthetic photometry is now available as part of the DR3 release of Gaia data products (Gaia Collaboration et al. 2022). We constructed a preliminary comparison between BV data from SD24 and the synthetic Gaia Synthetic Photometry Catalog (GSPC) photometry. We found from 230 stars with $V \leqslant 15$ that the SD24 $(B-V)$ colors are 0.009 ± 0.031 redder than the GSPC colors, an unconcerning difference. The ground-based V magnitudes are -0.034 ± 0.026 brighter than the synthetic magnitudes (i.e., SD24 – GSPC $= -0.034$). This comparison was constructed using only GSPC magnitudes without flags. A similar comparison using the standard photometry of Stetson (2000) in M67 relative to the GSPC data produces $\Delta V = -0.017 \pm 0.015$ (sd) from 542 stars.

With few independent determinations of foreground reddening and [Fe/H], the range of values under consideration remains large, $E(B-V) = 0.08 \pm 0.04$ and -0.35 ± 0.1. We adopt a value of $E(B-V) = 0.07$. The BV photometry from SD24 for NGC 2204, filtered by membership determinations from CG18, is shown in Figure 4 with scaled-solar Victoria-Regina (VR) isochrones (VandenBerg et al. 2006), adopted to allow direct comparison with the results for the previously analyzed metal-deficient clusters NGC 2506 (Anthony-Twarog et al. 2016, 2018b) and NGC 2243 (Anthony-Twarog et al. 2021). For consistency with the standard adopted in our previous cluster analyses using VR isochrones, we first zero the isochrones by requiring that a star of solar mass and metallicity at an age of 4.6 Gyr have $M_V = 4.84$ and $B-V = 0.65$, leading

[9] The WIYN Observatory was a joint facility of the University of Wisconsin-Madison, Indiana University, Yale University, and the National Optical Astronomy Observatory.

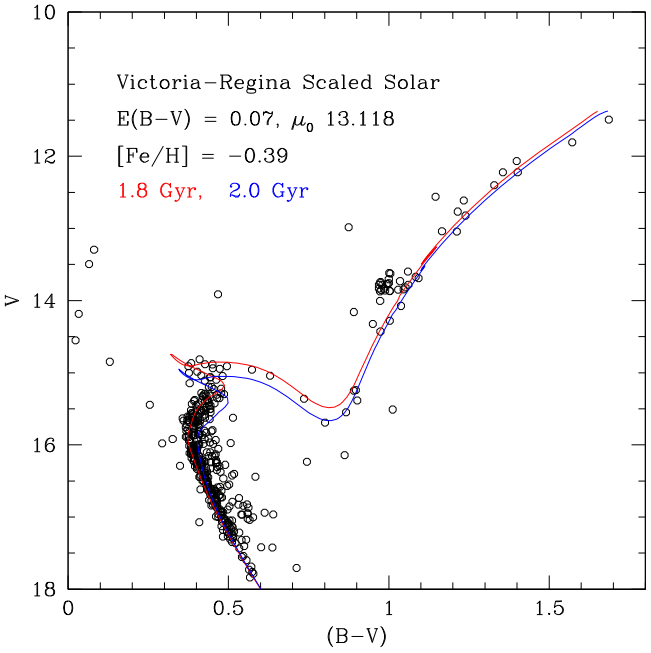

Figure 4. *BV* photometry from SD24 presented with VR isochrones, [α/Fe] = 0.0 and [Fe/H] = −0.39. The isochrones have been adjusted for a reddening value $E(B-V) = 0.07$ and a true distance modulus = 13.12, as derived from astrometry by CG20.

to the minor adjustments $\Delta V = 0.02$ and $\Delta(B-V) = +0.013$ mag. Displayed are 1.8 and 2.0 Gyr isochrones for [Fe/H] = −0.39, to which adjustments have been applied consistent with true distance modulus $\mu = 13.118$ (CG20) and $E(B-V) = 0.07$. From the quality of the match at the turnoff color and the simultaneous position of the subgiant branch luminosity, the implicit age of NGC 2204 is 1.85 ± 0.05 Gyr. Comparable fits, including the simultaneous agreement of giant branch and turnoff color, subgiant branch luminosity level, and accurate representation of the turnoff hook morphology, are obtained at a slightly higher reddening value ($E(B-V) = 0.08$) for a lower metallicity ([Fe/H] = −0.45) and a slightly lower reddening ($E(B-V) = 0.06$) for higher metallicity ([Fe/H] = −0.35). With the distance modulus largely fixed by astrometry, reddening shifts fold directly into the age determination and therefore produce morphological contradictions outside of these bounds.

5. Hydra Spectroscopic Analysis

5.1. Spectroscopic Processing with ROBOSPECT

Since the first cluster analysis in this series for NGC 3680 (Anthony-Twarog et al. 2009), where a modest number of dwarf stars and a few giants were considered, our approach has evolved as sample sizes have grown and new tools become available. Since 2015 (Lee-Brown et al. 2015), we have utilized an automated line-measurement program, ROBOSPECT (Waters & Hollek 2013), to replace exclusive dependence on manual measurement of line equivalent widths (EWs) as input to traditional LTE model atmosphere analysis via MOOG (Sneden 1973).[10] Lee-Brown et al. (2015) describe in considerable detail the various tests to which ROBOSPECT has been subjected. For the current investigation, each spectrum was individually corrected in ROBOSPECT for its unique radial velocity and run through 25 iterations of continuum fitting and line estimation using a Gaussian line profile with 3σ automatic line identification and no least-squares line deblending. All other parameters for the program were set to default values.

Table 2
Lines Used with Results from Giant Stars

λ (Å)	Element	log *gf*	Median EW (mÅ)	N_{Star}	[X/H]	MAD
6597.56	Fe	−1.018	57	47	−0.27	0.08
6627.54	Fe	−1.561	35	47	−0.44	0.04
6646.93	Fe	−4.032	31	43	−0.34	0.04
6653.91	Fe	−2.519	22	23	−0.32	0.04
6677.99	Fe	−1.574	146	4	−0.46	0.04
6703.57	Fe	−3.058	74	47	−0.39	0.06
6710.32	Fe	−4.767	58	47	−0.47	0.06
6725.36	Fe	−2.276	27	44	−0.41	0.07
6726.67	Fe	−1.105	56	47	−0.42	0.07
6733.15	Fe	−1.539	32	46	−0.42	0.07
6750.15	Fe	−2.775	104	47	−0.54	0.06
6806.86	Fe	−3.200	63	47	−0.45	0.05
6810.27	Fe	−1.085	60	47	−0.37	0.07
6820.37	Fe	−1.184	54	47	−0.32	0.10
6837.01	Fe	−1.848	29	44	−0.24	0.06
6717.68	Ca	−0.208	134	12	−0.11	0.05
6721.85	Si	−1.013	42	47	−0.26	0.08
6643.63	Ni	−1.926	131	32	−0.54	0.06
6767.77	Ni	−2.159	114	42	−0.57	0.06
6772.31	Ni	−0.948	66	47	−0.45	0.07

The potential line list in our chosen region (6400–6800 Å) includes over a dozen relatively isolated iron lines and a few lines of silicon, nickel, and calcium. Lines with EW larger than 150 mÅ are not used, out of concern that they exceed the linear portion of the curve of growth. Weak lines should also be excluded if their EW is near or below the anticipated EW error for a given line width and S/N, estimated from a formulation originally posed by Cayrel de Strobel (1988) and reformulated by Deliyannis et al. (1993). For stars with typical line width and S/N ∼ 100, 1σ error is ∼5 mÅ, suggesting exclusion of EW values below 15 mÅ. Our final line list contains 20 lines of interest (15 Fe, 3 Ni, 1 Ca, 1 Si), presented along with the relevant atomic parameters in Table 2. All of these lines are generally present and measurable in the cooler stars but very few stars near the turnoff have as many as four iron lines above an anticipated 2σ threshold of 10 mÅ, therefore metal abundance determinations will not be attempted for individual stars in this class.

To minimize external variables that might result from fiber-to-fiber variations and/or secular changes in the instrument's sensitivity, we reevaluate solar log *gf* values for each run and spectrograph setup by tuning those values to recreate solar abundances in daytime sky spectra, obtained in the appropriate fiber configuration for that purpose. Our evaluation of EW values to produce line-by-line abundance estimates is carried out in the context of model atmospheres generated by linear interpolation between Kurucz (1995) atmospheric models using MOOG's (Sneden 1973) *abfind* driver. We employ the 2014 LTE version of MOOG, for which the solar iron abundance is set at 7.50. In subsequent discussions, the solar A(Fe)[11] value

[10] Available at http://www.as.utexas.edu/~chris/moog.html.

[11] $A(X) = \log N_X - \log N_H + 12.00$.

Table 3
Revised H15 Color–Temperature Relations

Class	Number a_0	$(B-V)_{min}$ a_1	$(B-V)_{max}$ a_2	Min. T_{eff} a_3	Max. T_{eff} a_4	Std. Dev. a_5
MS/MSTO	99	0.21	1.51	7734	3618	139
⋯	8099.9436	−4343.1089	959.1094	256.6719	−39.6315	52.6089
SGB/RGB	72	0.43	1.62	6478	3602	100
⋯	7702.3968	−3601.1812	695.6553	431.7820	−12.5042	−194.4370

Note. $T_{eff} = a_0 + a_1X + a_2X^2 + a_3X \times [Fe/H] + a_4[Fe/H] + a_5[Fe/H]^2$.

will be subtracted from the MOOG abundance for each determination, yielding [Fe/H] relative to the Sun. For solar abundance checks, we employ a model constructed with (T_{eff}, log g, ξ) = (5770 K, 4.40, 1.14 km s^{-1}), where ξ denotes the microturbulent velocity parameter.

5.2. Atmospheric Parameters: T_{eff}, Surface Gravity, and Microturbulent Velocity

In the past we have used color–temperature relations from Ramírez & Meléndez (2005) and Deliyannis et al. (2002) for giants and dwarfs respectively. Because of its rich sample of over 150 stars and a homogeneous compilation of direct temperatures, Huang et al. (2015, H15) will be adopted going forward, with a few modifications. We want to prioritize disk metallicities and stars inside a T_{eff} range of 3600–7800 K, so some stars outside those limits were eliminated. We also reassigned luminosity class for the stars using absolute magnitudes with the help of Gaia parallaxes and photometric values from H15. The relations from H15 do not cover likely subgiants.

159 stars were sorted into clear main-sequence (MS) stars, evolved stars near the MSTO, probable SG stars, and clear RGB stars. To provide adequate color range and continuity between these classes, fits between T_{eff}, unreddened $(B-V)$ color, and [Fe/H] were made for 99 stars comprising 87 MS stars and 12 MSTO stars, then for 72 stars including 60 RGs, 6 SGs, and the evolved stars near the MS. The fits, with dependent variables of color and metallicity, are patterned after those used by H15 except that T_{eff} rather than $\theta = 5040/T_{eff}$ is solved for. The equations for RG/SG and MS/MSTO classes, color, and temperature limits are summarized in Table 3.

For our Hydra analysis, photometry from SD24 is used for all except a few stars outside the areal coverage of that study; for these the synthesized GSPC photometry has been adopted. A reddening of $E(B-V) = 0.07$ and [Fe/H] = −0.4 were chosen for the color–temperature conversions.

Estimates of surface gravity (log g) were obtained by direct comparison of V magnitudes and $(B-V)$ colors to the scaled-solar VR isochrones with [Fe/H] = −0.39 near 1.9 Gyr in age. For stars not immediately adjacent to the isochrone curve, adjustments were made to the nearest isochrone point of similar color and temperature based on the magnitude difference between the isochrone and the star such that $\Delta\log g = \Delta \log V/2.5$. For the comparison, $(m-M)_0 = 13.118$ and $E(B-V) = 0.07$ were applied to a 2.0 Gyr isochrone. Input estimates for ξ were constructed using the formulation by Bruntt et al. (2012) for stars within the valid ranges of log g and T_{eff}. For the most luminous giants with log $g \leqslant 2$, $\xi = 2.0 - 0.2$ log g.

Comparisons of our T_{eff} determinations relative to past work have been constructed, beginning with the infrared photometric studies by Houdashelt et al. (1992). These authors explored *JHK* colors to establish clearer pictures of clusters' reddening, distances, ages, and metallicities, developing profiles of cluster giant branches and building on preestablished indications of [Fe/H] and reddening. In this context, they studied giants in NGC 2204, making use of the earlier estimates of 0.08 for $E(B-V)$ and −0.35 for [Fe/H] from photometric studies by Dawson (1981) and Hawarden (1976a). As such, this is less an independent confirmation of our color–temperature scale than a check on it based on longer-wavelength photometry. From seven giants that are both cluster members and within the temperature bounds of the revised H15 color–temperature relation, the Houdashelt et al. (1992) temperatures are 30 ± 71 K (sd) warmer.

Similarly, Jacobson et al. (2011) provide atmospheric parameters for a group of 13 giants for which the median [Fe/H] is −0.26. The temperature scale is not independently determined from the spectra, but is based on photometry, a literature value for $E(B-V) = 0.08$, and the color–temperature relation of Alonso et al. (1999). The T_{eff} values for Jacobson et al. (2011) are on average 5 ± 93 K cooler than those derived herein from the revised H15 color–temperature calibration and *BV* photometry.

The spectroscopic study by Carlberg et al. (2016) is significant because the authors were able to derive T_{eff} entirely from spectroscopy in the established manner, i.e., normalizing the trend of A(Fe) with excitation potential. They also had sufficient spectral coverage and resolution to include both neutral and ionized iron lines, enabling an independent derivation of log g.

Excluding the likely binary W4119 = WOCS1003, our log g values are lower than those of Carlberg et al. (2016) by a modest 0.26 on average. An offset of this size has a minor impact on our abundances and no effect on our conclusions. By contrast, comparison of Carlberg et al. (2016)'s derived temperatures for most stars with $(B-V)$ colors, whether from Kassis et al. (1997) or SD24, shows a very similar slope to the H15 color–temperature relation but they are considerably hotter. If the worst outliers (WOCS4007 and 7014) are excluded, the average difference in T_{eff} in the sense (RevisedH15 − Carlberg) is −152 ± 33 K. We note that if the H15 color–temperature relation were to be preserved at [Fe/H] = −0.40, the foreground reddening $E(B-V)$ would have to be considerably higher, nearly 0.14, to produce temperatures this high. The two outliers for which a potential discrepancy between T_{eff} and photometric color is suggested will be revisited later in this paper.

By contrast, comparison of atmospheric parameters for some of the brighter cluster stars as determined in the Gaia DR3

Table 4
[Fe/H] for Giants, in Order of Increasing V magnitude

WOCS ID	[Fe/H]	N	MAD	$T_{\rm eff}$ (K)	log g	ξ
1006	−0.42	14	0.19	3805	1.0	1.80
1017	−0.30	14	0.04	4074	1.4	1.72
1028	−0.30	14	0.04	4147	1.5	1.70
4014	−0.41	14	0.08	4069	1.4	1.72
2028	−0.38	14	0.08	4194	1.6	1.68
1011	−0.38	14	0.06	4542	1.8	1.64
1002	−0.35	14	0.05	4369	1.8	1.64
3011	−0.40	14	0.05	4405	1.8	1.64
6014	−0.32	14	0.11	4359	1.8	1.64
2009	−0.38	13	0.03	5142	2.3	1.72
3006	−0.45	13	0.07	4502	2.0	1.60
2007	−0.36	13	0.03	4411	2.0	1.60
2016	−0.50	13	0.08	4721	2.4	1.62
1003	−0.33	14	0.07	4850	2.4	1.62
1010	−0.41	14	0.07	4841	2.4	1.62
1004	−0.41	14	0.05	4670	2.4	1.62
2003	−0.40	14	0.08	4651	2.4	1.62
2010	−0.35	13	0.09	4852	2.4	1.63
7014	−0.60	11	0.10	4775	2.4	1.62
2023	−0.34	13	0.07	4911	2.5	1.60
1019	−0.47	13	0.08	4852	2.5	1.59
3003	−0.40	13	0.06	4911	2.5	1.60
3009	−0.44	13	0.06	4868	2.5	1.59
8027	−0.37	13	0.04	4859	2.5	1.59
8014	−0.48	13	0.04	4922	2.5	1.60
4733	−0.41	14	0.06	4719	2.4	1.62
1736	−0.51	13	0.06	4897	2.5	1.59
3005	−0.36	13	0.04	4922	2.5	1.60
3015	−0.34	14	0.07	4886	2.5	1.59
4003	−0.42	13	0.08	4752	2.5	1.58
4007	−0.68	10	0.15	4788	2.5	1.58
5008	−0.47	13	0.04	4906	2.5	1.59
7028	−0.33	14	0.06	4877	2.5	1.59
4018	−0.35	14	0.08	4846	2.5	1.59
3016	−0.39	14	0.06	4846	2.5	1.59
6008	−0.36	13	0.06	4913	2.6	1.56
8028	−0.36	13	0.06	4913	2.6	1.56
5003	−0.30	14	0.04	4769	2.6	1.54
6021	−0.34	14	0.06	4846	2.7	1.51
5015	−0.54	12	0.02	4966	2.8	1.49
8011	−0.42	13	0.06	4911	2.8	1.48
8008	−0.37	11	0.04	5090	3.3	1.32
9020	−0.36	14	0.09	5104	3.2	1.37
8005	−0.40	13	0.10	5078	3.2	1.36
14011	−0.27	14	0.10	5161	3.3	1.34

parameter pipeline GSP-phot (Andrae et al. 2023) is much harder to understand. The GSP-phot $T_{\rm eff}$ values have a less coherent relationship with $(B-V)$ colors and are, on average, $\sim 200 \pm 266$ K higher, although the large dispersion in the individual differences makes this statistic hard to employ. Gaia GSP-phot also derives log g, nearly identical to values derived here from isochrones and photometry but with a sizeable standard deviation of 0.36 on that nearly null difference.

5.3. Metal Abundance Determinations

Model atmospheres were constructed for member giants using the grid of ATLAS9 models crafted by Kurucz (1995) for the input $T_{\rm eff}$, log g, and ξ listed in Table 4. We continue to use Kurucz models, though we have taken advantage of expanded model availability with [Fe/H] values now extending from −5.0 to 1.0. Our access to the models was via the online repository,[12] which was updated in 2014 and 2018. We construct models from simple linear interpolation of models with bracketing $T_{\rm eff}$ and log g values.

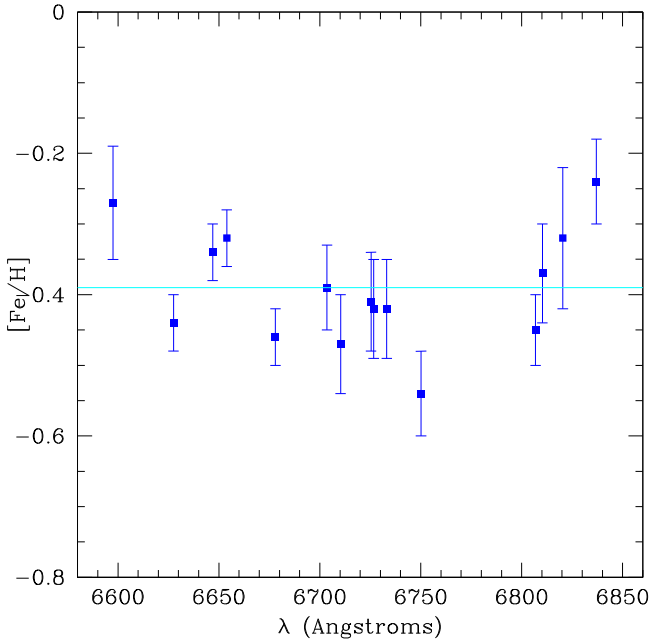

Figure 5. Abundance estimates for individual Fe lines. Results are shown for RG/SG members only. Error bars show MAD statistics

Each star's measured equivalent widths and model serve as input to the *abfind* routine of MOOG to produce individual [X/H] estimates for each measured line of element X for each star, and thus produce hundreds of separate abundance measures for single member stars of NGC 2204 with up to 15 [Fe/H] values for each star.

Our discussion utilizes median statistics to avoid the awkwardness of averaging logarithmic quantities. The median absolute deviation (MAD) is a robust indicator of dispersion among individual values. For typical distributions without extreme outliers, a traditional standard deviation is $\sim 1.48 \times$ MAD.

Our large number of 703 [Fe/H] estimates from 45 evolved stars is reduced to 627 if EW values below 15 or above 150 mÅ are excluded from further analysis. As is typical for median statistics considering large samples, modest changes in filtering have little consequence. The median [Fe/H] based on all eligible lines is -0.40 ± 0.08, where the error quoted is the MAD statistic, implying a more traditional standard deviation of 0.12. If the median of all 45 separate stellar abundance estimates is considered, the results are predictably similar: -0.38 ± 0.06 (MAD) for EW measures meeting the cutoffs described above. Presentation of results in Table 4 includes the $T_{\rm eff}$, log g, and ξ estimates for each evolved member star, while results specific to individual lines were included in Table 2. Among the evolved stars summarized in Table 4, two stars happened to be observed in separate configurations, spanning both years, 2014 and 2015, thus providing an opportunity to verify the repeatability of our [Fe/H] determinations. Results for these two stars differ by ∼0.05 dex.

In Figures 5 and 6, we illustrate the Fe abundance information by line wavelength and stellar $T_{\rm eff}$. For the 45

[12] http://kurucz.harvard.edu/grids/

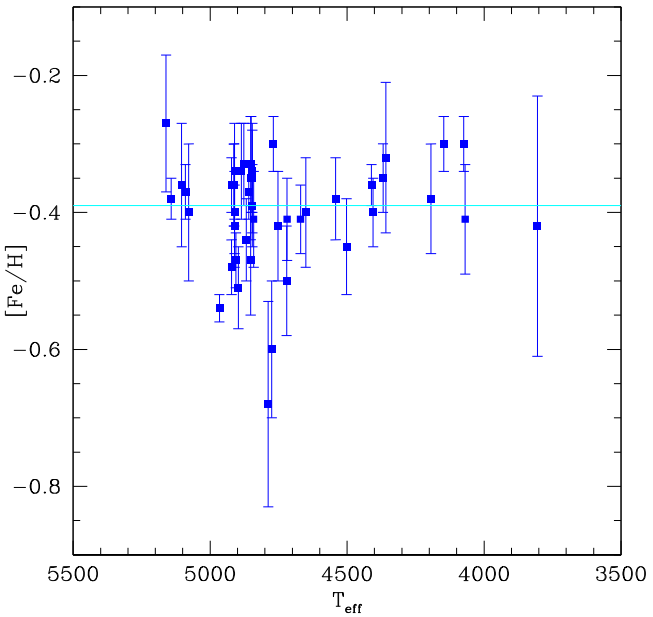

Figure 6. Estimates for [Fe/H] for individual RG/SG stars as a function of $T_{\rm eff}$. Error bars show the MAD statistic.

giants discussed above, stellar abundance estimates are based on 10–14 lines, with 13 lines being the median value. Two of the lowest [Fe/H] values occur for stars with fewer than 12 lines measurable. These stars, WOCS7014 and WOCS4007, have atypically large MAD values and are also the two stars previously noted to have spectroscopic temperatures inconsistent with their $(B-V)$ colors, according to Carlberg et al. (2016). If, as indicated by those spectroscopic temperatures, photometry assigns temperatures to these stars that are too low, a spuriously low metal abundance would be derived as a result, by as much as 0.15 dex for the star with the most discrepant temperature. We reiterate that this discrepancy between spectroscopic and photometric temperatures is not the exclusive result of use of photometry from A. Steinhauer et al. (2024, in preparation), Carlberg et al. (2016) uses photometry from Kassis et al. (1997) and notes the same issue. We further stress that retention of results for these two stars does not affect the overall abundance results for the cluster, due to the use of median statistics.

Our limited results for elements other than Fe are included in Table 2, with values for [m/H] accompanied by the number of evolved stars' lines and the MAD statistic for each median value. The relatively small number of star lines included for Ca is due to the typically large EW for this line in cooler stars. The results for Ca and Si imply slight α-enhancement. For a cluster $[{\rm Fe/H}] = -0.40$, $[{\rm Si/Fe}] = 0.14 \pm 0.12$ and $[{\rm Ca/Fe}] = 0.29 \pm 0.07$, where the errors noted here are standard deviations based on the MAD statistics. The median value for [Ni/H] from all lines is −0.52, implying $[{\rm Ni/Fe}] = -0.12 \pm 0.10$ (sd). With similar precepts for the determination of atmospheric parameters, ROBOSPECT was run on the more than 50 MS and MSTO stars. Unfortunately, the warm, relatively metal-weak and often broadened spectra produced far fewer than 15 successfully measured Fe lines in all but 14 stars. Even for these, only 4–6 lines were measurable, suggesting that a star-by-star analysis would be ineffective. Considering all of the Fe determinations en masse, from 50 eligible Fe lines among the 14 stars, a median value of −0.19 was derived for [Fe/H] with a large MAD statistic of 0.39. At best, these results may be considered weakly consistent with the larger sample and clearer results from SG and RGB stars.

What are the consequences of an incorrectly adopted reddening for the derived [Fe/H]? An inappropriately high reddening value assigns a higher than needed $T_{\rm eff}$ to the star, forcing a higher derived [Fe/H] value. For giant stars with [Fe/H] values near −0.40, the sensitivity of derived [Fe/H] values to adopted $E(B-V)$ is ∼0.015 for each increment of 0.01 in adopted $E(B-V)$. Fortunately, derived [Fe/H] values are less sensitive to the accuracy of the model atmospheres' assumed [Fe/H] values: an increment of 0.2 in model [Fe/H] produces a spurious increment of $\leqslant$0.05 in derived [Fe/H].

6. Li: Abundance Estimation and Evolutionary Implications

6.1. Li from Spectrum Synthesis

The challenge in estimating the abundance of Li is dominated by the fact that only one line near 6707.8 Å is accessible for analysis. While this is not a problem for lines of adequate strength, for hotter stars where the line strength weakens with increasing $T_{\rm eff}$ and/or for stars with rapid rotation where line broadening creates a wide but shallow profile that is difficult to define relative to the continuum, measuring the equivalent width can be an exercise in futility that, at best, only permits upper limits. Adding to the challenge is the existence of a weak Fe I line at 6707.4 Å, which, with inadequate resolution, can blend with the Li line to create an enhanced equivalent width for Li if not accounted for. Fortunately, this last issue is of minor importance due to the low metallicity of NGC 2204.

While the Li line's equivalent width can be measured noninteractively using ROBOSPECT or interactively using *splot* in IRAF, as in past analyses in the cluster series, we have chosen to use spectrum synthesis to define the individual stellar abundances—a critical approach for stars where the Li line is weak to nonexistent. The procedure as laid out in previous papers is as follows: each candidate star's spectrum is compared to the relevant model atmosphere using the *synth* driver in MOOG. When the model $T_{\rm eff}$ has been appropriately chosen, lines other than Li show consistent levels of agreement between spectrum and model, where "consistency" presumes that the line profile characterizing the spectrum is also appropriately modeled in MOOG. The line profile incorporates the known instrumental line width (0.55 mÅ for Hydra spectra) as well as corrections for limb-darkening (coefficient taken uniformly to be 0.5) and broadening due to rotation, for which projected rotational velocities may be interactively altered.

For all completed syntheses in the Li line region, the rotational velocity that appears to best fit the observed spectrum was recorded as well as the resulting A(Li) value. These $v_{\rm ROT}$ values were uniformly consistent with values obtained directly from the *fxcor* procedure described in Section 2.2 that determines both radial and rotational velocity parameters for values between 15 and 40 km s^{-1}. For the low end of the velocity scale the instrumental resolution limits the measurable velocities to between 5 and 10 km s^{-1}. Projected rotational velocities determined from *fxcor* analysis for all stars with Li detections or estimated upper limits are included with the A(Li) values presented in Table 5.

Table 5
Synthesis Results for Lithium

WOCS ID	v_{ROT}	σ_{vrot}	A(Li)	WOCS ID	v_{ROT}	σ_{vrot}	A(Li)
2014	11.3	0.9	−0.40	3016	10.7	0.3	⩽0.70
1006	4.4	0.3	−0.10	6008	11.1	0.3	⩽0.50
1017	5.0	0.2	⩽−1.50	8028	13.9	0.4	⩽0.60
1028	12.8	0.4	⩽−0.70	5003	16.1	0.4	1.05
4014	13.9	0.6	0.15	6021	18.0	0.4	1.10
2028	12.1	0.4	0.40	5015	19.8	0.5	⩽0.50
1011	14.3	0.4	⩽0.10	8011	21.1	0.5	1.20
1002	15.1	0.5	⩽−0.70	8008	17.8	0.4	1.30
3011	17.5	0.5	⩽−0.20	9020	18.6	0.5	1.30
6014	12.6	0.4	0.55	8005	19.9	0.5	1.30
2009	19.2	0.5	⩽0.70	12007	30.2	1.2	2.80
3006	13.9	0.4	⩽0.00	15013	41.8	1.7	2.75
2007	12.8	0.4	0.60	12015	30.3	1.3	3.00
2016	12.9	0.4	⩽0.10	14011	20.8	0.4	⩽0.70
1003	10.4	0.3	1.20	10019	41.1	1.6	2.85
1010	15.7	0.4	⩽0.40	15024	20.6	0.6	2.10
1004	14.0	0.4	1.00	13004	36.5	2.5	2.70
2003	12.8	0.4	1.00	20024	23.6	0.8	2.80
2010	17.4	0.4	⩽0.50	19014	10.4	0.3	2.70
7014	11.0	0.4	⩽0.60	33024	47.6	2.9	3.00
2023	12.8	0.4	⩽0.70	19023	25.3	1.1	2.75
1019	16.7	0.4	⩽0.50	17026	23.8	1.0	2.80
3003	15.2	0.4	⩽0.60	C	21.2	1.0	2.80
3009	15.1	0.4	⩽0.80	20012	21.1	1.0	2.70
8027	14.8	0.4	⩽0.60	24014	18.6	0.7	2.85
8014	17.5	0.5	⩽0.60	19020	20.2	0.8	2.95
4733	15.3	0.4	1.20	17008	21.6	1.2	3.00
4009	35.0	⋯	1.10	16017	22.8	0.8	⩽2.10
1736	15.8	0.4	⩽0.60	20009	27.6	1.1	2.60
3005	15.9	0.4	⩽0.60	24021	25.7	1.8	⩽2.30
3015	13.2	0.3	⩽0.70	20008	32.7	1.2	⩽2.10
4003	19.7	0.6	1.00	27021	26.6	0.9	⩽2.10
4007	11.3	0.5	⩽0.60	29018	18.8	0.6	⩽2.00
5008	13.2	0.4	⩽0.70	25011	13.5	0.6	⩽2.40
7028	8.40	0.2	⩽0.50	36028	26.8	1.4	⩽2.10
4018	19.2	0.5	⩽0.60	E	21.0	0.8	⩽2.00

For cases in which the Li line is distinct and clearly present, an abundance for Li is discerned by comparing the fit for different A(Li) values. In many cases, the Li line is not obviously distinguishable from noise or nearby spectral features; in these cases, an upper limit is determined by noting the value of A(Li) below which changes to the spectrum-model fit are no longer distinguishable. A(Li) determinations, including upper limits, for all measurable spectra are listed in Table 5.

6.2. Li Evolution and the CMD: Evolved Stars

Figure 7 shows the CMD for evolved stars with Li detections and Li upper limits. Two stars, WOCS1005 and WOCS2006 (open circles), require some clarification since synthesis was not possible due to the stars' extremely low temperatures. WOCS2006, flagged for potential binarity and variability, is the reddest star in the sample, past the "dog-leg" of the giant branch. Although too cool for synthesis, it does have a conspicuous Li line with an EW of over 240 mÅ. WOCS1005 has a similar spectrum with dominant molecular bands, yet no obvious Li line.

The next coolest star, WOCS1017, has a measurable though more modest Li EW of 29 mÅ, but synthesis appears to suggest an implausibly low upper limit. The other cool stars for which Li was not detected all have Li line EWs from ROBOSPECT of

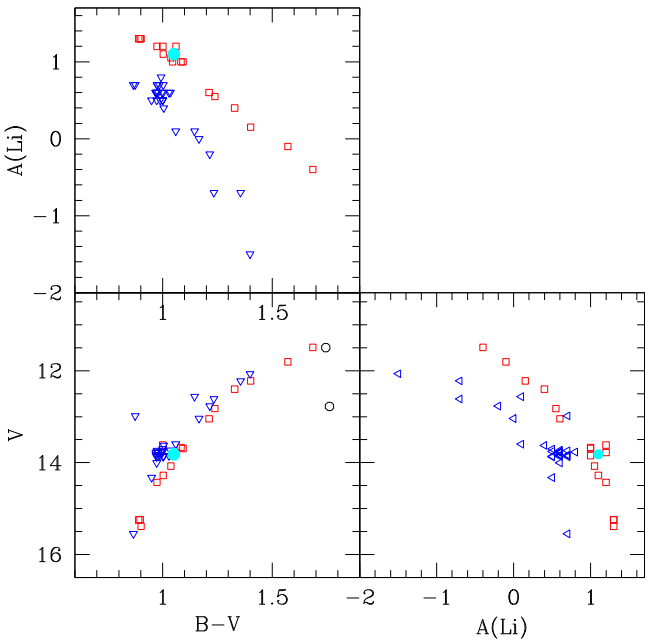

Figure 7. Li abundance patterns among the giants. The location of WOCS4009 is shown with a cyan dot. Blue triangles indicate upper limits to A(Li) while red squares illustrate detections.

10 mÅ or less if the contribution of the adjacent Fe line is estimated and subtracted.

One of the striking features of Figure 7 is the separation of the red giants into clear detections (red squares) versus stars for which only upper limits are derivable (blue triangles). All the stars that define the red boundary in the CMD delineating the first-ascent red giant (FRG) branch have measurable Li, starting with A(Li) just below the canonical prediction of 1.4 at the base of the giant branch and declining to −0.4 near the tip of the giant branch. While it may go lower beyond this point, as discussed earlier, the two coolest stars fall outside the $T_{\rm eff}$ limits of the synthetic spectra. By contrast, with only one exception, the red clump giants (RCGs) only have upper limits centered on $A(\mathrm{Li}) = 0.6 \pm 0.2$ and typically 0.5 dex below the measured detections for FRG at the same luminosity. Thanks to the precision photometry of SD24, for stars brighter than the RCGs the Li bifurcation translates into a color separation where the bluer stars all have distinctly lower A(Li) limits than the detections on the RCGs at the same luminosity.

It should be emphasized that this bifurcation is not an artifact of the spectrum synthesis approach. The separation for the giants above the clump is at least as distinct if only Li EWs are considered. For the stars with Li upper limits, EWs are uniformly low, 20–26 mÅ. This measured EW includes the contribution from the nearby Fe line, with an estimated strength of 10–20 mÅ going up this part of the RGB. In contrast, the six giants with Li detections have Li EWs from 60 to 120 mÅ, larger for the cooler stars. The separation in the CMD of these giant classes above the level of the RGB clump is subtle but believable, leading to the prediction that the bluer stars are post-RGC, asymptotic giant branch (AGB) stars evolving back up the giant branch. In support of this interpretation, we note that one of the upper limit stars, WOCS3011 = W2212, was selected for observation by Carlberg et al. (2016) with the expectation that it was an AGB star, an assignment confirmed by their determination of the AGB separation in the $T_{\rm eff}$–log g diagram. Unfortunately, no other stars among our group of cool stars with upper limits for Li were observed by Carlberg et al. (2016).

The results presented in Figure 7 include photometry and an Li abundance for WOCS4009 (cyan filled circle), for which the only spectroscopic data are those of the VLT spectrum shown in Figure 3. Because of its location in the CMD between the RGC and the FRG branch it is impossible to determine which category describes the star. Although synthesis is difficult for such wide lines, an abundance of $A(\mathrm{Li}) = 1.1$ is suggested by comparison to a model spectrum broadened by 35 km s^{-1}. The model was constructed in the same manner as for the other giants, adopting $T_{\rm eff} = 4743$ K, $\log g = 2.5$, and $\xi = 1.58$ km s^{-1}. Plausible estimates for the actual equatorial rotational velocity for WOCS4009 are considerably higher. For a radius of $\sim 12\,R_\odot$, as suggested by the isochrones, and the observed period from ASAS-SN of 6.18 days, an equatorial rotational velocity $\geqslant$100 km s^{-1} is implied. If WOCS4009 is a member of the RGC, it is clearly Li-rich compared to the typical RGC star, though its record as a photometric variable and potential radial velocity variable makes its history and evolutionary status tricky to discern. It appears to be another example of a growing class of giant stars with discordant Li abundances found in anomalous positions in the CMD and/or with broad-lined spectra and photometric variability associated with rapid rotation, such as W7017 in NGC 6819 (Anthony-Twarog et al. 2013), star 4128 in NGC 2506 (Anthony-Twarog et al. 2018b), star W2135 in NGC 2243 (Anthony-Twarog et al. 2020, 2021), and, most recently, star 4705 in NGC 188 (Sun et al. 2022). To date, only W7017 has been confirmed as a low-mass RGC star, despite its position in the CMD redward of the FRG branch (Carlberg et al. 2015). With a luminosity at the level of the RGC, a broad-line spectrum, and photometric variability, supposedly due to rotation, on timescales of 6–7 days, WOCS4009 closely resembles star W2135 in NGC 2243.

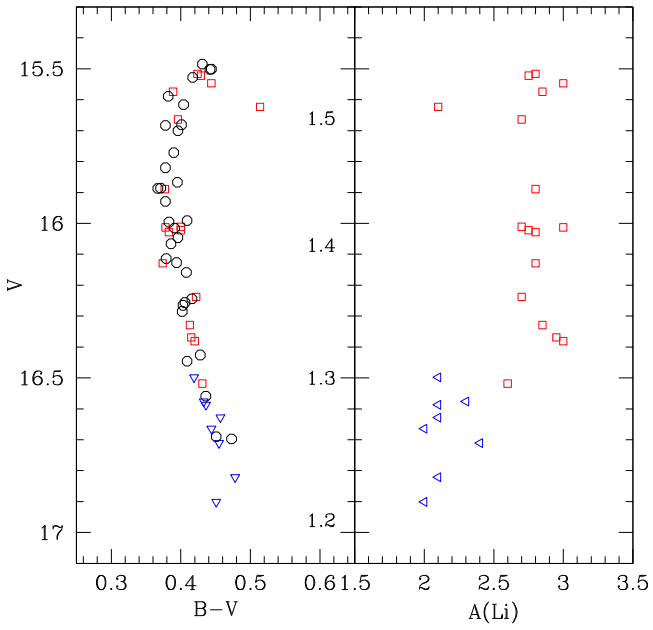

Figure 8. Li abundance patterns among MSTO stars. As before, red and blue symbols show stars with detected Li or upper limits. Black symbols show the CMD location for stars with no successful synthesis measurement of Li. Numbers to the right of the CMD in the left panel show the stellar masses in solar units at the corresponding magnitude levels, based on isochrones of Figure 4.

6.3. Li Evolution and the CMD: MSTO Stars

Figure 8 shows the trends of A(Li) with $(B-V)$ color and V magnitude for MSTO stars in NGC 2204. The stars for which synthesis could not be carried out are designated with open black symbols, while the other symbols have the same meaning as in Figure 7. For the stars with usable spectra, the A(Li) pattern is straightforward with A(Li) remaining constant at 2.85 ± 0.15 between $V = 15.5$ and 16.5. The only exception is the one star evolving into the subgiant branch with $A(\mathrm{Li}) \sim 2.1$ en route to the base of the giant branch, by which time its A(Li) will have dropped to just below 1.4. However, at the critical boundary of $V = 16.5$, one sees the distinct transition to the Li-dip, bottoming out at an upper limit of $A(\mathrm{Li}) = 2.0$.

In the similar anticenter cluster NGC 2243, the center of the main-sequence Li-dip is located at $\sim 1.15 \pm 0.02\,M_\odot$, with the transition to undepleted Li abundances at the high-mass end, the "wall," appearing over the range between 1.21 and $1.24\,M_\odot$. Extrapolating these masses for a slightly more metal-rich cluster (Δ[Fe/H] = +0.15 dex) implies adding $0.06\,M_\odot$ to these feature masses based upon an [Fe/H]-based slope of 0.4 (Anthony-Twarog et al. 2021). The expectation is that the wall in NGC 2204 should be positioned between 1.27 and $1.30\,M_\odot$. Using the VR isochrones shown in Figure 4, the mass associated with each V magnitude at the MSTO is plotted

along the central vertical axis of Figure 8. While the number of stars defining the edge is limited in comparison with the comparable plot for NGC 2243, it is apparent that the transition between $V = 16.5$ and 16.6 is consistent with the predicted mass range and clearly higher than the mass identified for the more metal-deficient NGC 2243. The expected low-mass limit of the Li-dip should occur near $1.15\,M_{\odot}$, fainter than the magnitude limit of the current survey, as confirmed by Figure 8.

6.4. Li Evolution: NGC 2204 and the Li Cluster Pattern

The Li trends with mass and evolutionary state, as laid out in Figures 7 and 8, are in qualitative agreement with expectations as delineated in past analyses of clusters of similar age and/or metallicity. Stars above the Li wall at the MSTO have a modest range in abundance but generally follow a distribution that peaks between $A(\mathrm{Li}) = 2.9$ and 3.4. Stars leaving the main sequence for the subgiant branch exhibit a steep decline in A(Li) with color, approaching a value typically below $A(\mathrm{Li}) = 1.4$ at the base of the giant branch. Between this point and the luminosity level of the RGC, the FRG branch shows at most a minor decline of ∼0.1 dex in A(Li). Beyond this point, A(Li) drops at an increasing rate as one approaches the tip of the FRG branch. Beyond this evolutionary point, the RGC stars, with a few key exceptions, exhibit only upper limits to A(Li), limits that fall below the measured values for the FRG at the same luminosity, in theory due to the prior effects of the He flash at the FRG branch tip.

The role of metallicity in defining the mass range of the Li-dip has already been noted. However, it also clearly plays a key role in defining the distribution of stars among the varied evolutionary phases from the MSTO and beyond, thereby altering the relative distribution of stars with differing Li signatures. The fraction of FRG branch stars populating the CMD from the blue edge of the subgiant branch to the luminosity level of the RGC is controlled primarily by stellar mass. Given [Fe/H], stars above a certain mass leaving the main sequence have convective cores such that H-exhaustion occurs simultaneously within an isothermal He core; the He core mass grows with time due to H-burning in a shell outside the core. However, if the core mass fraction rises above approximately 10%, core collapse ensues and the star evolves rapidly in T_{eff} to reach the base of the vertical FRG branch, creating the Hertzsprung gap. As core contraction continues and the core temperature rises, He-ignition finally occurs under nondegenerate conditions.

For stars of lower mass, the size of the convective zone within the core declines with decreasing mass until the core is totally radiative. Under these circumstances, the fractional mass of the totally He core region grows with time, but fails to reach the critical 10% boundary before the star becomes partially degenerate. The presence of degenerate gas supplies an alternative means of support, which allows the star to evolve more slowly from the MSTO across the subgiant branch to the base of the vertical FRG branch. The burning H shell slowly adds mass to the He core, moving the star up the FRG branch until He ignites under degenerate conditions. The slower rate of evolution leads to well-populated subgiant and vertical FRG branches, as exemplified by the classic old disk cluster M67 (see, e.g., Figure 7 of Twarog et al. 2023). It should be noted, however, that the transition to lower-mass stars not only leads to better delineation of the subgiant branch, but also weakens the fractional population of the RGC and the RG branch (FRG and AGB combined) above the luminosity of the RGC. Compare, e.g., the distribution of RG stars for NGC 2204, as exemplified by Figure 4, with a similar plot for NGC 2243 at 3.6 Gyr (Figure 4 of Anthony-Twarog et al. 2021). Ignoring stars positioned well off the evolutionary tracks in the CMD, NGC 2204 exhibits approximately the same number (∼12) of giants above (FRG and AGB) as below the luminosity of the clump. By comparison, similar counts for NGC 2243 produce a ratio of 8 (23) to 1 (3) in favor of stars below the clump. As for the actual number of stars within the clump, the approximate number is 15 for NGC 2204 as opposed to 6 for NGC 2243. Equally relevant, for NGC 2204, all but two of the stars below the RGC and half those above it have detectable Li. One potential RGC star might have detectable Li. In NGC 2243, none of the RGC or red giants brighter than the RGC have detectable Li, while only half below the RGC do. Clearly the greater age of NGC 2243 dramatically alters the evolutionary distribution of the evolved stars and their Li distribution.

However, age must not be the only impactful factor, as illustrated by a direct comparison of NGC 2204 with NGC 2506, a cluster of apparently identical age (1.85 Gyr) but slightly higher [Fe/H] (−0.27) (Anthony-Twarog et al. 2016, 2018b). As shown in Figure 5 of Anthony-Twarog et al. (2018b), the single-star FRG branch ($(B - V)$ above 0.6) of NGC 2506 contains 31 stars to the luminosity level of the RGC, all but seven of which have measurable Li. Only three stars sit above the level of the clump, two of which lie well to the blue of the expected FRG branch and only have upper limits for A(Li). Approximately two dozen stars populate the RGC; only one has detectable Li. These numbers/distributions should be contrasted with the distinctly different character laid out above for NGC 2204.

In fact, NGC 2204 morphologically leans toward the younger (1.5 Gyr) but more metal-rich ([Fe/H] ∼ −0.1) cluster NGC 7789 (Brunker et al. 2013; S. W. Brunker et al. 2024, in preparation). This richly populated cluster has only six single FRG stars below the level of the clump compared to 21 FRG and AGB stars above it and a dominant 56 single stars within the RGC. The fact that NGC 2204 looks morphologically younger than NGC 2506, a cluster of the same age but higher metallicity, is consistent with the pattern defined by the main-sequence Li-dip. As discussed earlier, the masses bracketing the main-sequence Li-dip decline by $0.04\,M_{\odot}$ for each drop of 0.1 dex in [Fe/H]. The impact of this shift to lower mass is that more metal-deficient clusters exhibit the same qualitative trend with Li as metal-rich clusters, just delayed in time. For example, while NGC 2243 (Anthony-Twarog et al. 2021) and M67 (Twarog et al. 2023) have almost the same age, the stars leaving the main sequence in the former cluster come from the hot side of the Li wall, while the stars populating the subgiant and giant branches in M67 came from well inside the Li-dip (Boesgaard et al. 2020). NGC 2243 will not reach the Li-dip/subgiant morphology of M67 for at least 0.5 Gyr. Since the metallicity differential between NGC 2506 and NGC 2204 is less than one-fourth that of M67/NGC 2243, one expects a much smaller morphological age differential when comparing them. Therefore, if the structural parameters that generate the metallicity dependence of the mass limits for the Li-dip are reflections of a more fundamental role of metallicity/mass controlling the post-main-sequence luminosity function among first- and second-ascent red giants, NGC 2204 should

morphologically resemble a younger NGC 2506 at the same CMD-based isochronal age. For completeness, it should be noted that one can simply make NGC 2204 younger by adopting a larger reddening of $E(B-V)=0.09$. This makes the turnoff bluer, leading to higher stellar $T_{\rm eff}$ and higher [Fe/H] by +0.03 dex. The revised age becomes 1.7 Gyr, though the quality of the fit to the isochrones is noticeably worse.

To close the cluster comparison, we turn to the issue of MSTO rotation speeds. As demonstrated initially for four clusters in Figure 11 in Deliyannis et al. (2019) and expanded to include NGC 2243 in Figure 11 of Anthony-Twarog et al. (2021), the distribution of rotation speeds for stars above the wall is a strong function of age and, like the Li-dip itself, metallicity. For a younger cluster of near solar metallicity such as NGC 7789, $v_{\rm ROT}$ extends from an observational minimum near 20 km s^{-1} to measurable limits approaching 100 km s^{-1}. For some stars with even higher assumed $v_{\rm ROT}$ the lines are too extended to allow plausible measurement. NGC 3680 (Anthony-Twarog et al. 2009), with a metallicity comparable to NGC 7789 but an estimated age of 1.75 Gyr, displays a much narrower range of $v_{\rm ROT}$ with all stars located below 50 km s^{-1}. By the 2.25 Gyr age of NGC 6819 and the 3.6 Gyr age of the very metal-deficient NGC 2243, all stars but one in each cluster have $v_{\rm ROT}$ below 25 km s^{-1}. By contrast, NGC 2506, with an age slightly greater than NGC 3680 but more metal-deficient, displays a $v_{\rm ROT}$ spread that is dominated by stars between 25 and 65 km s^{-1}, but reaches to almost 100 km s^{-1}, much more similar to NGC 7789. Completing the pattern, Figure 8 shows that more than half the stars above $V=16.5$ (open circles) have no measured Li limit or detection. The stars that are plotted on the right side of Figure 8 have $v_{\rm ROT}$ that ranges from the system limit of ~20 km s^{-1} to just under 50 km s^{-1} (Table 5). The inability to measure $v_{\rm ROT}$ for the open circles of Figure 8 stems from the same problem already noted for a subsample of stars in NGC 7789: the typical line is spread over such a wide range in wavelength that a plausible measure of its true width becomes debatable. While some of the stars without $v_{\rm ROT}$ measures may be unresolved binaries composed of equal-mass stars, especially given the almost vertical nature of the MSTO, the fraction of open circles is too large to be explained this way, especially given the analysis of similar samples in other clusters. Continuing the pattern laid out above for the post-main-sequence morphology, we conclude that the $v_{\rm ROT}$ distribution for NGC 2204 is similar to that for NGC 2506 but, because of its lower metallicity at the same age, is more heavily weighted toward $v_{\rm ROT}$ above 50 km s^{-1}, leaning toward a distribution more comparable to NGC 7789. Because of the lower [Fe/H], the weaker lines may become less discernible at $v_{\rm ROT}$ above 50 km s^{-1}. As a crude test of this hypothesis use was made of the one line that remains strong, sometimes too strong, for the hot stars populating the vertical turnoff on NGC 2204: Hα. Using the interactive routine *splot*, within IRAF, a Lorentzian profile was matched to the Hα line in each spectrum. For the stars with measurable $v_{\rm ROT}$ in Table 5, the average FWHM of the line was determined to be 4.85 ± 0.40 Å. For the stars where the line strengths were deemed too shallow to supply a plausible A(Li) measure, the comparable FWHM is 5.93 ± 0.97 Å. For the extreme cases where no metal lines can be readily measured, FWHM becomes 6.62 ± 0.65 Å.

6.5. NGC 2204 and Galactic Li Evolution

The metallicity of a cluster clearly impacts the evolution of Li within the cluster as a function of mass, particularly at intermediate and lower masses. Equally relevant is the manner in which cluster metallicity is tied to the initial Li abundance of the cluster. It has been recognized for decades that with a primordial A(Li) near 2.7 and a solar value at 3.3 (Asplund et al. 2009; Spite et al. 2012), A(Li) must increase with time via contributions from stellar sources. Since the mean Galactic [Fe/H] has increased from almost 0 to solar and higher over the same interval, it is generally assumed that A(Li) and [Fe/H] should be roughly correlated, a pattern confirmed by a variety of cluster and field studies (see, e.g., Gao et al. 2020; Randich et al. 2020) and the discussion in Anthony-Twarog et al. (2018b). How does NGC 2204 fit within the metallicity trend? For NGC 2506 ([Fe/H] = −0.27), the mean A(Li) among the stars at the vertical turnoff is 3.05 ± 0.02 (sem) from 71 stars. While some stars do scatter above the solar system value of 3.3, it is clear that the stars on the hot side of the Li-dip are systematically lower in the mean than expected for solar metallicity (Anthony-Twarog et al. 2021). At the other end of the metallicity scale, NGC 2243 ([Fe/H] = −0.54) has a much smaller range in V for the stars on the hot side of the Li-dip, consistent with its older age. However, among this limited sample, only one star has A(Li) greater than 3.0 and the range for stars above the Li-dip extends to A(Li) ~ 2.0 (Anthony-Twarog et al. 2021). Clearly NGC 2243 has a lower mean A(Li) than NGC 2506. For NGC 2204 ([Fe/H] = –0.40), the mean A(Li) for stars on the hot side of the Li-dip is 2.83 ± 0.03 (sem) from 15 stars. Keeping in mind that the sample size is modest and stars with significant rotation could not be evaluated for Li, it is still the case that no star at the turnoff of NGC 2204 outside the Li-dip has A(Li) above 3.0, and the full A(Li) range extends from 3.0 to 2.7, significantly smaller than found in NGC 2506 at the same age.

7. Summary

The focus of the current investigation has been the metal-deficient, moderately old open cluster NGC 2204. High-dispersion spectroscopy of 167 stars, selected primarily to map the evolutionary change in Li from the MSTO to the FRG branch, has provided unusual insight into the broader question of how stellar metallicity, mass, and age can impact the observed distribution of A(Li) among evolving stars within the Galactic disk. After eliminating astrometric and radial velocity nonmembers, including unfortunately the majority of stars positioned between the MSTO and the FRG branch at the level of the clump, as well as probable binaries, EW analysis of hundreds of Fe lines in 45 evolved stars with narrow line profiles generates a mean metallicity of $[{\rm Fe/H}]=-0.40\pm0.12$ (sd). Given the number of stars/lines included in the cluster average, the dominant uncertainty in the abundance remains the zero-point of the absolute [Fe/H] scale through the uncertainty in $E(B-V)$ and ultimately the $T_{\rm eff}$ scale, though there is universal agreement that the reddening in the direction of NGC 2204 is low, consistent with the adopted value of $E(B-V)=0.07$. The derived cluster abundance places NGC 2204 almost exactly midway between the more metal-rich NGC 2506 (Anthony-Twarog et al. 2016, 2018b) and the more metal-poor NGC 2243 (Anthony-Twarog et al. 2021).

The complications that make the MSTO abundance analyses significantly more challenging for a cluster like NGC 2204 are twofold: (a) at lower [Fe/H], stars at a given $T_{\rm eff}$ generally have weaker metallic lines, and (b) stars of lower [Fe/H] at a given age near the MSTO are generally hotter. Added to these issues is the unexpected discovery that a significant fraction of the stars at the MSTO for NGC 2204 exhibit higher than expected rotation speeds, in many cases making any attempt at line measurement impossible.

With the basic stellar parameters in hand, spectrum synthesis was carried out for all cluster members where line broadening due to rotation was small enough to allow adequate evaluation of the impact of varying the Li line strength. This proved feasible for all the post-MSTO stars, but allowed A(Li) estimation for less than half (24 of 56) of the stars at or below the MSTO. For the red giants, the A(Li) pattern is familiar, but striking. At the base of the vertical FRG branch, A(Li) falls just below the canonically predicted Li-rich boundary for giants at 1.4. As stars evolve up the FRG branch, measurable A(Li) drops steadily to a limiting value below −0.4 for the star at the tip of the FRG branch. Two stars lie just beyond this tip limit, but the cool $T_{\rm eff}$ and the spectroscopic complexity make model synthesis almost impossible. At best, one can say that these stars appear to be more Li-deficient than the hotter stars, but just how deficient is uncertain. With one exception, the stars within the RGC exhibit upper limits to A(Li) that are lower than the detectable values for the FRG branch stars at the same luminosity as the clump. If these stars evolve from the population at the red giant tip, the true upper limits for the RGC stars should be $A(\mathrm{Li}) = -0.4$ or lower, a limit that is simply beyond the capacity of our spectra for stars at the $T_{\rm eff}$ of the clump.

Perhaps the most striking feature of the A(Li) CMD distribution among the evolved stars is the separation of stars above the clump into two distinct categories of detection versus upper limit, where the stars with upper limits all lie brighter/bluer than the stars with detections. With two exceptions that sit well above the FRG branch, the separation in color/luminosity is small, but the photometric precision is high enough to accept this separation as real. The obvious explanation for this bluer band is that they represent post-RGC stars evolving up the giant branch a second time, i.e., they are AGB stars. The spectroscopic analysis of one of these stars by Carlberg et al. (2016) supports its AGB status.

The giant population of NGC 2204 also contains an example of a persistent anomaly appearing consistently among older clusters with a sufficient population of stars, giants with rapid rotation, and/or anomalous Li for their supposed position within the CMD (see Anthony-Twarog et al. 2020; Sun et al. 2022 for recent comprehensive discussions of this phenomenon). Since the spectrographic line signature makes the measurement of $v_{\rm ROT}$ below $\sim$15 km s^{-1} virtually impossible, it is expected that the mean for all giants should scatter close to this value. As detailed in Section 2.2, it does. However, one star, WOCS4009 (see Figure 3), clearly has anomalously broadened lines compared to the typical effect found in most giants, implying a speed near 35 km s^{-1}. Evolved stars with $v_{\rm ROT}$ speeds above 30 km s^{-1} are rare, consistently making up less than 1% of the K giants found in the field (Carlberg et al. 2011; Tayar et al. 2015). The challenges to understanding these stars are multiple. First, if a star is a rapid rotator as a giant, did it start out that way on the main sequence and simply fail to spin down along the path of normal post-main sequence evolution or was there a physical mechanism that caused a normal giant to spin up? In both cases, the common solution remains interaction/mass transfer with a binary companion (see, e.g., the discussion of short-period, tidally locked binaries in Deliyannis et al. 2019). For NGC 2204, unlike NGC 2243, the $v_{\rm ROT}$ distribution of stars at the MSTO appears dominated by stars undergoing rapid rotation, thereby providing a ready source of potential candidates for a progenitor that is a rapid rotator. Additionally, NGC 2204 has a modest supply of blue stragglers, commonly accepted as the products of mass transfer within a binary. Second, the evaluation of these stars is complicated by the fact that anomalous evolution likely positions them within the CMD in locations inconsistent with their actual internal state when compared to isochrones for normal single stars. Star W7017 in NGC 6819 remains a prime example (Anthony-Twarog et al. 2013; Carlberg et al. 2015). The lack of clarity regarding evolutionary phase clouds its classification as an Li-rich giant since one must first answer "rich relative to what"? If WOCS4009 is an FRG, its A(Li) is consistent with the other stars in this evolutionary phase. If it is in the RGC, it is clearly Li-rich. This categorization is further clouded by the fact that, as a metal-deficient cluster, the primordial A(Li) for NGC 2204 appears to be closer to 2.85 than the solar metallicity reference value of 3.3. If Li is reduced by the same factor predicted for stars of solar metallicity, the initial value at the base of the FRG branch should be 1.0 or less, rather than 1.4.

To close, the fundamental value of NGC 2204 remains its ability to illuminate the roles metallicity and age play within the evolution of Li for stars evolving on and after the main sequence. The trends defined and/or enhanced by past cluster studies within this series have included the shift in the position of the Li-dip with decreasing mass as [Fe/H] declines, i.e., the mass boundary of the Li wall, the narrowing of the spread in $v_{\rm ROT}$ among stars on the hot/high-mass side of the Li wall as a cluster ages, and the correlated spread in A(Li) for the same hot/high-mass stars while still on the main sequence and prior to entering the subgiant branch, again emphasizing that A(Li) does not remain constant for stars above the Li wall. With the addition of NGC 2204 to the cluster mix, a direct comparison is possible to a cluster of identical age (1.85 Gyr) but higher metallicity, NGC 2506. The contrast between the two, supposedly dominated by the difference in metallicity, reveals that the stars on the hot side of the wall are more heavily weighted toward rapid rotators than those in NGC 2506 and that the post-MSTO luminosity function shows a distribution of giants more heavily weighted toward FRG branch stars above the RGC than below, with a richer population of RGC stars, while NGC 2506 has almost no stars above the level of the RGC and the majority of this small sample has no detectable Li, possibly indicating AGB status. From the previously identified patterns, NGC 2204 more closely resembles what one expects for a younger NGC 2506, i.e., closer in appearance to the more metal-rich ([Fe/H] ~ -0.1) but younger (1.5 Gyr) cluster NGC 7789. This trend is analogous to what is seen in the comparison between two clusters of much older, but similar, age ($\sim$3.6 Gyr), NGC 2243 ([Fe/H] = −0.54) and M67 ([Fe/H] = +0.03) (Anthony-Twarog et al. 2021; Twarog et al. 2023). Stars leaving the main sequence in M67 are emerging from the cool side within the Li-dip while the stars populating the subgiant branch in NGC 2243 are still

originating above the wall of the Li-dip. Thus, metallicity appears to have a broader and more nuanced impact on the distribution of stellar properties on the main sequence and beyond, over and above the simple one of setting the mass boundaries for the Li-dip, an effect that is generally downplayed or ignored in the analysis of field star distributions.

Acknowledgments

NSF support for this project was provided to B.J.A.-T. and B.A.T. through NSF grant AST-1211621, and to C.P.D. through NSF grants AST-1211699 and AST-1909456. Extensive use was made of the WEBDA database maintained by E. Paunzen at the University of Vienna, Austria (http://www.univie.ac.at/webda).

This research has made use of the ESO Science Archive Facility and refers to observations collected at the European Southern Observatory under ESO program 188.B-3002(V).

Dr. Donald Lee-Brown assisted with observations and processing. The authors are grateful for the always excellent support provided by the WIYN telescope staff that made this research possible. We are also appreciative of the helpful and specific comments made by the referee, which have strengthened the paper.

Facility: WIYN

Software: IRAF (Tody 1986), MOOG (Sneden 1973), LACOSMIC (van Dokkum 2001), ROBOSPECT (Waters & Hollek 2013), TOPCAT (Taylor 2005).

ORCID iDs

Barbara J. Anthony-Twarog https://orcid.org/0000-0001-8841-3579
Constantine P. Deliyannis https://orcid.org/0000-0002-3854-050X
Aaron Steinhauer https://orcid.org/0000-0002-5719-5596
Qinghui Sun https://orcid.org/0000-0003-3281-6461
Bruce A. Twarog https://orcid.org/0000-0001-5436-5206

References

Alonso, A., Arribas, S., & Martinez-Roger, C. 1999, A&AS, 140, 261
Andrae, R., Fouesneau, M., Sordo, R., et al. 2023, A&A, 674, 27
Anthony-Twarog, B. J., Deliyannis, C. P., Harmer, D., et al. 2018a, AJ, 156, 37
Anthony-Twarog, B. J., Deliyannis, C. P., Rich, E., & Twarog, B. A. 2013, ApJL, 767, L19
Anthony-Twarog, B. J., Deliyannis, C. P., Twarog, B. A., Croxall, K. V., & Cummings, J. D. 2009, AJ, 138, 1171
Anthony-Twarog, B. J., Deliyannis, C. P., & Twarog, B. A. 2016, AJ, 152, 192
Anthony-Twarog, B. J., Deliyannis, C. P., & Twarog, B. A. 2020, AJ, 160, 75
Anthony-Twarog, B. J., Deliyannis, C. P., & Twarog, B. A. 2021, AJ, 161, 159
Anthony-Twarog, B. J., Lee-Brown, D. B., Deliyannis, C. P., & Twarog, B. A. 2018b, AJ, 155, 138
Anthony-Twarog, B. J., Twarog, B. A., & McClure, R. D. 1979, ApJ, 233, 188
Asplund, M., Grevasse, N., Sauval, A. J., & Scott, P. 2009, ARA&A, 47, 481
Bertelli, G., Bressan, A., Chiosi, C., Fagotto, F., & Nasi, E. 1994, A&AS, 106, 275
Boesgaard, A. M., Lum, M. G., & Deliyannis, C. P. 2020, ApJ, 888, 28
Boesgaard, A. M., & Tripicco, M. 1986, ApJL, 302, L49
Brunker, S. W., Anthony-Twarog, B. J., Deliyannis, C. P., & Twarog, B. A. 2013, BAAS, 221, 250.28
Bruntt, H., Basu, S., Smalley, B., et al. 2012, MNRAS, 423, 122
Cantat-Gaudin, T., Anders, F., Castro-Ginard, C., et al. 2020, A&A, 640, A1
Cantat-Gaudin, T., Jordi, C., Vallenari, A., et al. 2018, A&A, 618, A93
Carlberg, J. K., Cunha, K., & Smith, V. V. 2016, ApJ, 827, 129
Carlberg, J. K., Majewski, S. R., Patterson, R. J., et al. 2011, ApJ, 732, 39
Carlberg, J. K., Smith, V. V., Cunha, K., et al. 2015, ApJ, 802, 7
Cayrel de Strobel, G. 1988, in IAU Symp. 132, The Impact of Very High S/N Spectroscopy on Stellar Physics, ed. G. Cayrel de Strobel & M. Spite (Dordrecht: Kluwer), 345
Christian, C. A., Heasley, J. N., & Janes, K. A. 1985, ApJ, 299, 683
Christian, C. A., & Janes, K. A. 1979, AJ, 84, 204
Cummings, J. D., Deliyannis, C. P., Anthony-Twarog, B. J., Twarog, B. A., & Maderak, R. M. 2012, AJ, 144, 137
Dawson, D. W. 1981, AJ, 86, 237
Deliyannis, C. P., Anthony-Twarog, B. J., Lee-Brown, D. B., & Twarog, B. A. 2019, AJ, 158, 163
Deliyannis, C. P., Pinsonneault, M. H., & Duncan, D. K. 1993, ApJ, 414, 740
Deliyannis, C. P., Steinhauer, A., & Jeffries, R. D. 2002, ApJL, 577, L39
Demarque, P., Woo, J.-H., Kim, Y.-C., & Yi, S. K. 2004, ApJS, 155, 667
Dias, W. S., Monteiro, H., Caetano, T. C., et al. 2014, A&A, 564, A79
Friel, E. D., Janes, K. A., Tavarez, M., et al. 2002, AJ, 124, 2693
Gaia Collaboration, Brown, A. G. A., Vallenari, A., et al. 2016, A&A, 595, A2
Gaia Collaboration, Brown., A. G. A., Vallenari, A., et al. 2018, A&A, 616, A1
Gaia Collaboration, Montegriffo, P., Bellazzini, M., et al. 2023, A&A, 674, A33
Gaia Collaboration, Vallenari, A., Brown, A. G. A., et al. 2023, A&A, 674, A1
Gao, Q., Lind, L., Amarsi, A. M., et al. 2020, MNRAS, 497, L30
Hawarden, T. G. 1975a, MNRAS, 173, 231
Hawarden, T. G. 1975b, MNRAS, 173, 801
Hawarden, T. G. 1976a, MNRAS, 174, 225
Hawarden, T. G. 1976b, MNRAS, 174, 471
Houdashelt, M. L., Frogel, J. A., & Cohen, J. G. 1992, AJ, 103, 163
Huang, Y., Liu, X. W., Yuan, H. B., Xiang, M. S., & Chen, B. Q. 2015, MNRAS, 454, 2863
Jacobson, H. R., Friel, E. D., & Pilachowski, C. A. 2011, AJ, 141, 58
Janes, K. A. 1979, ApJS, 39, 135
Kassis, M., Janes, K. A., Friel, E. D., & Phelps, R. L. 1997, AJ, 113, 1723
Kurucz, R. L. 1995, in IAU Symp. 149, The Stellar Populations of Galaxies, ed. B. Barbuy & A. Renzini (Dordrecht: Kluwer), 225
Lee-Brown, D. B., Anthony-Twarog, B. J., Deliyannis, C. P., Rich, E., & Twarog, B. A. 2015, AJ, 149, 121
McClure, R. D., Forrester, W. T., & Gibson, J. 1974, ApJ, 189, 409
McClure, R. D., Twarog, B. A., & Forrester, W. T. 1981, ApJ, 243, 841
Mermilliod, J. C., & Mayor, M. 2007, A&A, 470, 919
Ramírez, I., & Meléndez, J. 2005, ApJ, 626, 465
Randich, S., Pasquini, L., Franciosini, L., et al. 2020, A&A, 640, L1
Rozyczka, M., Kaluzny, J., Krzemiński, W., & Mazur, B. 2007, AcA, 57, 323
Schlafly, E. F., & Finkbeiner, D. P. 2011, ApJ, 737, 103
Schlegel, D. J., Finkbeiner, D. P., & Davis, M. 1998, ApJ, 500, 525
Shappee, B. J., Prieto, J. L., Grupe, D., et al. 2014, ApJ, 788, 48
Sneden, C. 1973, ApJ, 184, 839
Spite, M., Spite, F., & Bonifacio, P. 2012, Li in the Cosmos, Mem. Soc. Astron. Italiana, Suppl., 22, 9
Steinhauer, A. 2003, PhD thesis, Indiana University
Sun, Q., Deliyannis, C. P., Twarog, B. A., et al. 2022, MNRAS, 513, 5387
Stetson, P. B. 2000, PASP, 112, 925
Tayar, J., Ceillier, T., García-Hernández, D. A., et al. 2015, ApJ, 807, 82
Taylor, M. B. 2005, in ASP Conf. Ser. 347, Astronomical Data Analysis Software and Systems XIV, ed. P. Shopbell, M. Britton, & R. Ebert (San Francisco, CA: ASP), 29
Tody, D. 1986, Proc. SPIE, 627, 733
Twarog, B. A., Anthony-Twarog, B. J., Deliyannis, C. P., & Steinhauer, A. 2020, Li in the Universe: to Be or not to Be, Mem. Soc. Astron. Italiana, 91, 74
Twarog, B. A., Anthony-Twarog, B. J., & Deliyannis, C. P. 2023, AJ, 165, 105
Twarog, B. A., Ashman, K. M., & Anthony-Twarog, B. J. 1997, AJ, 114, 2556
van Dokkum, P. G. 2001, PASP, 113, 1420
VandenBerg, D. A., Bergbusch, P. A., & Dowler, P. D. 2006, ApJS, 162, 375
Waters, C. Z., & Hollek, J. K. 2013, PASP, 125, 1164